







# A new form of axonal pathology in a spinal model of neuromyelitis optica

Marina Herwerth,<sup>1,2,†,‡</sup>  Selin Kenet,<sup>1,3,†</sup> Martina Schifferer,<sup>4,5</sup> Anne Winkler,<sup>6</sup>  Melanie Weber,<sup>1,§</sup> Nicolas Snaidero,<sup>1</sup> Mengzhe Wang,<sup>1</sup> Melanie Lohrberg,<sup>6</sup> Jeffrey L. Bennett,<sup>7</sup>  Christine Stadelmann,<sup>6</sup>  Bernhard Hemmer<sup>2,5</sup> and Thomas Misgeld<sup>1,4,5</sup>

<sup>†</sup>These authors contributed equally to this work.

See Bradl (<https://doi.org/10.1093/brain/awac141>) for a scientific commentary on this article.

Neuromyelitis optica is a chronic neuroinflammatory disease, which primarily targets astrocytes and often results in severe axon injury of unknown mechanism. Neuromyelitis optica patients harbour autoantibodies against the astrocytic water channel protein, aquaporin-4 (AQP4-IgG), which induce complement-mediated astrocyte lysis and subsequent axon damage.

Using spinal *in vivo* imaging in a mouse model of such astrocytopathic lesions, we explored the mechanism underlying neuromyelitis optica-related axon injury.

Many axons showed a swift and morphologically distinct ‘pearls-on-string’ transformation also readily detectable in human neuromyelitis optica lesions, which especially affected small calibre axons independently of myelination. Functional imaging revealed that calcium homeostasis was initially preserved in this ‘acute axonal beading’ state, ruling out disruption of the axonal membrane, which sets this form of axon injury apart from previously described forms of traumatic and inflammatory axon damage. Morphological, pharmacological and genetic analyses showed that AQP4-IgG-induced axon injury involved osmotic stress and ionic overload, but does not appear to use canonical pathways of Wallerian-like degeneration. Subcellular analysis demonstrated remodelling of the axonal cytoskeleton in beaded axons, especially local loss of microtubules. Treatment with the microtubule stabilizer epothilone, a putative therapy approach for traumatic and degenerative axonopathies, prevented axonal beading, while destabilizing microtubules sensitized axons for beading.

Our results reveal a distinct form of immune-mediated axon pathology in neuromyelitis optica that mechanistically differs from known cascades of post-traumatic and inflammatory axon loss, and suggest a new strategy for neuroprotection in neuromyelitis optica and related diseases.

- 1 Institute of Neuronal Cell Biology, Technical University of Munich, Munich, Germany
- 2 Department of Neurology, Klinikum rechts der Isar, Technical University of Munich, Munich, Germany
- 3 Graduate School of Systemic Neurosciences, Ludwig-Maximilians University, Munich, Germany
- 4 German Center for Neurodegenerative Diseases (DZNE), Munich, Germany
- 5 Munich Cluster of Systems Neurology (SyNergy), Munich, Germany
- 6 Institute of Neuropathology, University Medical Center Göttingen, Göttingen, Germany
- 7 Departments of Neurology and Ophthalmology, Programs in Neuroscience and Immunology, University of Colorado School of Medicine, Aurora, USA

<sup>‡</sup>Present address: Institute of Pharmacology and Toxicology, University of Zurich, Zurich, Switzerland

Received July 07, 2021. Revised January 31, 2022. Accepted February 12, 2022. Advance access publication February 24, 2022

© The Author(s) 2022. Published by Oxford University Press on behalf of the Guarantors of Brain.

This is an Open Access article distributed under the terms of the Creative Commons Attribution-NonCommercial License (<https://creativecommons.org/licenses/by-nc/4.0/>), which permits non-commercial re-use, distribution, and reproduction in any medium, provided the original work is properly cited. For commercial re-use, please contact [journals.permissions@oup.com](mailto:journals.permissions@oup.com)

<sup>§</sup>Present address: Department of Cardiovascular Surgery, German Heart Center Munich, Technical University of Munich, Germany

Correspondence to: Thomas Misgeld  
 Technical University of Munich  
 Institute of Neuronal Cell Biology (TUM-NCB)  
 Biedersteiner Strasse 29, 80802 München, Germany  
 E-mail: thomas.misgeld@tum.de

**Keywords:** neuromyelitis optica; aquaporin-4; astrocytopathy; neuroinflammation; neurodegeneration

**Abbreviations:** AQP4-IgG = aquaporin-4-specific autoantibodies; CFP = cyan fluorescent protein; GFP = green fluorescent protein; OFP = orange fluorescent protein; NMO = neuromyelitis optica

## Introduction

In many neurological diseases, damage to axons plays a central role in pathology. In some conditions, such as neurodegeneration or multiple sclerosis, axon injury is insidious and slowly progressive. In other diseases, e.g. trauma and stroke, axons are damaged in a cataclysmic event. In the former conditions, the optimal strategy to prevent axon injury appears to be early disease modulation, while acute neuroprotection and neuroregeneration need to be prioritized in the latter.

Neuromyelitis optica (NMO), which is part of a spectrum of antibody-mediated autoimmune CNS disorders,<sup>1,2</sup> presents a blend of these disease dynamics. In patients with NMO, astrocytes are the primary target of aquaporin-4-specific autoantibodies (AQP4-IgG).<sup>3–5</sup> Astrocyte injury is swiftly followed by demyelination and neuronal pathology.<sup>6,7</sup> The resulting disease is characterized by relapses, and unlike in multiple sclerosis, disease progression is rarely observed between attacks.<sup>8,9</sup> Instead, even the first inflammatory lesions typically inflict irreparable damage to axons in the eponymous fibre tracts of spinal cord and optic nerve. Thus, devising early neuroprotective interventions would be an important addition to emerging immunomodulatory therapies,<sup>10,11</sup> which only allow blunting further damage once the diagnosis is established and the initial damage has occurred. In addition to these specific therapeutic needs, AQP4-IgG-positive NMO also represents a paradigmatic example of an ‘astrocytopathy’.<sup>12,13</sup> As astrocyte damage is increasingly implicated in more common neuroinflammatory and neurodegenerative diseases,<sup>14–20</sup> understanding how axon injury emerges as a consequence of astrocyte dysfunction is of general importance.

Thus far, the mechanisms of axon injury in NMO have mostly been inferred from neuropathological analysis.<sup>21</sup> Possible mechanisms of axon injury in NMO include inflammatory bystander damage via complement,<sup>22</sup> as well as ionic, ischaemic or excitotoxic mechanisms driven by astrocytic loss.<sup>21</sup> In addition, previously established programs of axon degeneration, such as Wallerian-like degeneration or focal axonal degeneration<sup>23–25</sup> have been implicated in NMO,<sup>7,26,27</sup> suggesting shared axon destruction pathways between NMO and neurodegeneration or multiple sclerosis. Still, no clear-cut axon injury program that could represent a suitable downstream target for neuroprotective interventions in NMO has been revealed.

We have previously established two-photon *in vivo* imaging of the mouse spinal cord as a suitable approach to model the dynamics of cellular injury in AQP4-IgG-induced lesions in mice.<sup>28</sup> In this model, astrocytes undergo lytic cell death after local application of NMO patient-derived AQP4-IgG and human complement to dorsal white matter tracts. Direct *in vivo* observation then reveals the

quick spread of pathology to other cell types, including neurons and their axons. We now explored the mechanisms of such axon injury and demonstrate that these changes—which closely mimic the axon pathology seen in NMO—are neither due to the known axon destruction programs, such as Wallerian-like axon loss or multiple sclerosis-related focal axonal degeneration, nor do they involve bystander injury via complement pores. Instead, axons in acute astrocytopathic lesions undergo a ‘beading’ phenomenon that thus far has not been characterized *in vivo*, which could be ameliorated by microtubule stabilization, a therapy strategy previously investigated in traumatic spinal cord injury<sup>29</sup>—suggesting a potential new target for neuroprotective intervention in NMO-related pathology.

## Materials and methods

### Animals

To image astrocytes, we used 2- to 5-month old male and female *Aldh1l1:green fluorescent protein (GFP)* mice obtained from MMRR [strain: Tg(*Aldh1l1-EGFP*)OFC789Gsat/Mmucd] and to image axons *Thy1:OFP3* mice,<sup>30</sup> courtesy of J. Lichtman (Harvard University, Cambridge, MA, USA). The *Thy1:TNXXL* strain—courtesy of O. Griesbeck (Max Planck Institute of Neurobiology, Martinsried, Germany)—was used to measure axonal calcium levels as previously described.<sup>31,32</sup> Providing the SARM knockout mouse line was a courtesy of A. Ding (Cornell University, Ithaca, NY, USA). Animal experiments were conducted in accordance with local regulations and were approved by the responsible regulatory agencies.

### Patient sera, antibodies and complement source

AQP4-IgG-positive NMO sera were collected from patients treated in the Department of Neurology, Klinikum rechts der Isar, Technical University of Munich, Germany. Samples were stored in the biobank of the Department, which is part of the Joint Biobank Munich in the framework of the German Biobank Node. Written informed consent was obtained from each participant. The study was approved by the ethics committee of the Technical University of Munich. All cases fulfilled the Wingerchuk diagnostic criteria for NMO.<sup>1</sup> Healthy donor plasma was used as a control (Ctrl-IgGs) and three different sera of healthy subjects obtained from the ‘blood bank’ of the Bavarian Red Cross were pooled and served as complement source. AQP4-IgG-positive NMO and Ctrl-IgG samples were heat-inactivated. In some experiments, a human IgG1 recombinant antibody rAQP4-IgG (clone 7-5-53) reconstructed from a clonotypic plasma blast obtained from the CSF of an

Table 1 Clinical data of NMO patients

Patient	B/A	Age/sex	Disease duration (years)	Serum AQP4-IgG	CNS region studied
1	B	37/female	9	positive	Occipital lobe
2	B	31/female	5	positive	Parietal lobe
3	B	57/male	10	positive	Parietal lobe
4	B	45/female	>2	positive	Spinal cord
5	B	42/male	10	positive	Frontal lobe
6	A	16/female	4	n/a	Pons
7	A	69/female	0.4	n/a	Pons

A = autopsy; B = biopsy; n/a = not available.

NMO patient was used.<sup>33</sup> The recombinant rCtrl-IgG (clone ICOS-5-2), a human IgG<sub>1</sub> antibody of unknown specificity from a meningitis patient, served as an isotype control. Side-by-side comparison of the astrocyte death rate and dynamics of axonal beading with human serum from NMO patients versus rAQP4-IgG ruled out unspecific effects that might occur from other autoantibodies potentially present in the human sera (data not shown).

## Human tissue

To investigate axonal pathology, we screened formalin-fixed and paraffin-embedded biopsy and autopsy tissue from the archives of the Institute of Neuropathology at the University Medical Centre Göttingen. The study was approved by the local ethics committee. Of the 18 NMO patients with tissues available (nine biopsies and nine autopsies), seven lesions fulfilled the criteria for analysis, i.e. lesions localized in white matter tracts with longitudinally running axons. The samples were classified as early lesions, defined by the presence of recently infiltrated MRP14 positive macrophages.<sup>34,35</sup> Only biopsies from patients that were later tested to be AQP4-IgG positive were included. The serological status was unknown in autopsied cases, as these NMO patients had died before AQP4-IgG testing was available. Neuropathologically, NMO was confirmed by the presence of inflammatory, demyelinating, macrophage-rich CNS-lesions with loss of GFAP- and AQP4-expressing astrocytes and relative axonal preservation (Table 1).

Biopsies used as controls contained—besides diseased areas, which were not analysed—neuropathologically normal white matter with axons that were assessable longitudinally. Except for one patient, autopsies showed no CNS pathology (Table 2).

Formalin-fixed paraffin-embedded tissue was cut into 1–2-µm thick sections and used for histological and immunohistochemical stainings. To investigate astrocyte loss, immunohistochemistry

was performed using antibodies directed against AQP4 (1:200, rabbit, Sigma Aldrich, #A5971) and GFAP (1:1000, rabbit, Dako, #A5971). LFB/PAS staining was used to detect demyelination, while MRP14 immunohistochemistry (1:500, mouse, Acris, clone S36.48, #BM4026) served to detect recently infiltrated macrophages. Axonal pathology in NMO lesions was investigated by immunohistochemistry for NF200 for overall presence of swellings (1:400, mouse, clone N52, Sigma Aldrich, #N0142), and by Bielschowsky silver impregnation for ‘pearls-on-string’ morphology (axons with multiple swellings) at ×400 magnification. Axonal morphologies were counted in NMO lesions and related to the lesion size as measured with the software ImageJ/Fiji.<sup>36,37</sup> On the same slide, axons in a fixed area the adjacent non-lesioned white matter were evaluated. Additionally, neuropathologically normal white matter of control patients was analysed. For NF200 immunohistochemistry, all beaded axons (also with single swellings) were quantified using a morphometric grid within the lesion, in the non-lesioned and in control white matter. All quantifications were performed at ×400 magnification in at least eight different fields of view and presented as counts per mm<sup>2</sup>.

## Mouse NMO model

### Surgical procedures

Laminectomy surgery was performed as previously described.<sup>24,28</sup> In brief, mice were anaesthetized by an intraperitoneal injection of medetomidin (0.5 mg/kg), midazolam (5 mg/kg) and fentanyl (0.05 mg/kg). Anaesthesia was reapplied as needed. After a double dorsal laminectomy over the third lumbar (L3) and L4 segments, mice were suspended using compact spinal cord clamps.<sup>38</sup> An imaging window free from dura was established in the imaging area using a bent hypodermic needle. To allow superfusion with artificial CSF (aCSF, in mM: 148.2 NaCl, 3.0 KCl, 0.8 Na<sub>2</sub>HPO<sub>4</sub>, 0.2 NaH<sub>2</sub>PO<sub>4</sub>, 1.4 CaCl<sub>2</sub> and 0.8 MgCl<sub>2</sub>), a well around the opening was built using 2–3% agarose.

### In vivo imaging

In vivo imaging of the lumbar spinal cord was performed as previously described.<sup>24,28,39</sup> Briefly, stacks were acquired using two-photon microscopes (Olympus FV1000 MPE or FVMPE-RS) tuned to 1000 nm to excite GFP and orange fluorescent protein (OFP) at the same time. The systems were equipped with a 25×/1.05 numerical aperture (NA) water-dipping cone objective. Emission was first filtered through a 690-nm short-pass dichroic mirror; to separate the GFP and OFP channels, we used a G/R filter set (BA495-540, BA570-625) mounted in front of gallium arsenide phosphide

Table 2 Clinical data of control patients

Patient	B/A	Age/sex	Neuropathological diagnosis	Cause of death	CNS region studied
1	B	76/male	Glioblastoma multiforme	n/a	Frontal lobe
2	B	78/male	Vasculitis	n/a	Frontal lobe
3	B	81/male	Glioblastoma multiforme	n/a	Temporal lobe
4	B	75/male	Multiple sclerosis	n/a	Corpus callosum
5	A	57/male	No CNS pathology	Cardiac arrest	Pons
6	A	57/female	No CNS pathology	Sepsis	Pons
7	A	39/female	No CNS pathology	Pulmonary embolism	Pons
8	A	65/male	TBI	Trauma	Pons
9	A	38/female	No CNS pathology	Breast carcinoma	Pons

A = autopsy; B = biopsy; n/a = not applicable; TBI = traumatic brain injury.

(GaAsP) photomultiplier tubes. For fluorescence resonance energy transfer signal imaging in *Thy1:TNXXL* mice, the laser was tuned to 840 nm and a cyan fluorescent protein (CFP)/or yellow fluorescent protein (YFP) cube (BA480/40, BA540/40) was positioned in front of GaAsP detectors to separate CFP and cpCitrine signals as previously described.<sup>32</sup> Time-lapse (xyzt) stacks were acquired at 10-min intervals for 6 h with the following parameters: 30–50 images (zoom 2.0; pixel size: 0.281  $\mu\text{m}$ ) at 1- $\mu\text{m}$  z-step intervals.

Diluted recombinant antibodies (rAQP4-IgG versus rCtrl-IgG ICOS-5-2; 1.5  $\mu\text{g}/\text{ml}$  respectively) or heat-inactivated plasma (AQP4-IgG versus Ctrl-IgG; 150  $\mu\text{g}/\text{ml}$  respectively) together with 20% of pooled healthy donor sera as a complement source was applied every 30 min for the first 2 h; afterwards the solution was refreshed every 60 min. Under these experimental conditions, we have previously shown that phototoxicity and transgenic labelling does not significantly influence the health of spinal axons.<sup>24,28,32,39</sup> TTX (1  $\mu\text{M}$ , Tocris) was washed in for 10 min before the start of the experiment. Mannitol (300 mM, Sigma) was solved in aCSF and applied continuously throughout the experiment to achieve a stable hyperosmolar condition (200% of the initial osmolarity). The pro-apoptotic drug HA-14 (1  $\mu\text{M}$ , Sigma), microtubule destabilizer Nocodazole (350  $\mu\text{M}$ , Tocris), or the vehicle (1.4% DMSO, Sigma) was applied continuously for the first 3 h of the experiments, which was followed by 1 h of treatment with hypo-osmolar solution (90% aCSF, diluted with  $\text{H}_2\text{O}$ ). Experiments with pharmacological manipulations were scored by a blinded observer.

### Fluorescence resonance energy transfer analysis

Data analysis was done as previously described.<sup>32</sup> Time-lapse recordings were first inspected as z-projected image stacks and putative changes from low to high calcium were marked. Each such calcium transition was individually verified in unprocessed three-dimensional (3D) image stacks. Only axons that were observable at least 50  $\mu\text{m}$  in length were included in the analysis. Local background was subtracted from each channel before calculating the cpCitrine/CFP ratio. Axons were scored as having elevated calcium levels if the cpCitrine/CFP ratio was 50% greater than at baseline (cf. Williams et al.<sup>32</sup>). Axonal calibre was measured as the diameter of individual axons in a representative area in unprocessed image stacks, using the Fiji plot profile plugin.

### Epothilone B administration

For local administration, vehicle alone (PEG 300, Sigma) or epoB (Selleckchem, 5  $\mu\text{g}/\text{ml}$ , dissolved in vehicle) was delivered during NMO experiments continuously via bath application from 30 min on until the end of the experiment (6 h) in double transgenic *Aldh1l1:GFP*  $\times$  *Thy1:OPF3* mice. For systemic administration, mice were intraperitoneally injected with 1.5 mg/kg BW epoB (dissolved in vehicle, 100  $\mu\text{l}$  volume) or vehicle alone 24 h before imaging experiments.<sup>29</sup> No abnormal behaviour or weight loss were observed in mice during this time period.

### Immunohistochemistry and confocal imaging

Mice were perfused transcardially with 4% paraformaldehyde (PFA) in 0.0.1 M phosphate-buffered saline (1  $\times$  PBS; in mM: 1.5  $\text{KH}_2\text{PO}_4$ , 2.7 KCl, 8.1  $\text{Na}_2\text{HPO}_4$  and 137 NaCl), followed by an additional overnight fixation in 4% PFA. Over the next days, whole mounts of lumbar spinal cord were extracted and kept in well plates filled with 1  $\times$  PBS for further staining procedures. Antibodies were diluted in 0.2% Triton X-100, 10% normal goat serum and 1% bovine serum

albumin in PBS. For tubulin staining, spinal cord tissue was incubated with  $\beta$ III-tubulin antibody (Alexa Fluor 488- or 647-conjugated, mouse; BioLegend, 1:200) for 6 days in whole-mount preparations or overnight for 100  $\mu\text{m}$  vibratome sections. Stained whole mounts of fixed spinal cords (2–4 spinal segments) were secured with the dorsal surface in contact with a cover glass in 2% agarose for imaging. Samples were scanned with an upright confocal microscope (Olympus FV1000) equipped with 20 $\times$ /0.8 NA and 60 $\times$ /1.42 NA oil-immersion objectives, as previously described.<sup>28,32</sup> For quantification, regions of interest were drawn around beadings, then the mean grey values within and between the beadings were measured for each axon, and averaged for every channel. Background subtraction was applied to each single optical section, and the ratio of the mean grey values for the tubulin staining and the OPF3 signal were used to normalize for cytoplasmic content. The analysis of epoB experiments in *Aldh1l1:GFP*  $\times$  *Thy1:OPF* mice was performed blinded to exclude observer bias.

### Electron microscopy

#### Transmission electron microscopy

The animals used for the transmission electron microscopy (EM) experiment were perfused directly after the experiment with 5 ml of HBSS, followed by 30 ml of fixative (2.5% glutaraldehyde, 4% PFA in phosphate buffer; 0.1 M). The spinal cord at the laminectomy site was immersed in the same solution during the perfusion. After overnight fixation, the spinal cord was extracted and further post-fixed overnight at 4°C in the same fixative. The area below the laminectomy was collected and post-fixed with 2%  $\text{OsO}_4$  and 1.5% ferricyanide (Science Services), dehydrated by ethanol, then acetone and finally Epon-embedded (Serva). Then 50-nm ultrathin sections from the area corresponding to the imaging site in the two-photon acute imaging experiment were contrasted with 4% uranyl acetate (Science Services) and lead citrate (Sigma). The imaging was done on a transmission electron microscope JEM 1400 plus (JEOL) equipped with an 8 megapixel camera (Ruby, JEOL). Large areas covering the first 20–30  $\mu\text{m}$  from the dorsal pial surface of the spinal cord were imaged using the Shuttle-and-Find software at  $\times 8000$ . Images were processed using the open-source image analysis software, Fiji.

#### Serial section electron microscopy using automated tape-collecting ultramicrotome

We applied a standard rOTO en bloc staining protocol including a tannic acid incubation step. Spinal cord cross sections (0.5 mm in thickness) were initially post-fixed in 2% osmium tetroxide (EMS), 1.5% potassium ferricyanide (Sigma) in 0.1 M sodium cacodylate (Science Services) buffer (pH 7.4). After three washing steps in buffer and water, the staining was enhanced by reaction with 1% thiocarbonylhydrazide (Sigma) for 45 min at 40°C. The tissue was washed in water and incubated in 2% aqueous osmium tetroxide, washed and further contrasted by 0.2% tannic acid for 30 min. After overnight incubation in 1% aqueous uranyl acetate at 4°C and 2 h at 50°C, Walton's lead aspartate treatment (L-aspartic acid, Sigma; lead nitrate, Alfa Aesar) was performed for 30 min at room temperature. The samples were dehydrated in an ascending ethanol series and infiltrated with Epon (medium hardness, Serva). To prevent folds, the dorsal part of the spinal cord cross section was supported by mouse cortex tissue.<sup>40</sup> The block was trimmed by 200  $\mu\text{m}$  at a 90° angle on each side using a TRIM90 diamond knife (Diatome) on an ATUMtome (Powertome, RMC). Consecutive sections were

taken with a 35° ultra-diamond knife (Diatome) at a nominal cutting thickness of 200 nm and collected on freshly plasma-treated (custom-built, based on Pelco easiGlow, adopted from M. Terasaki, U. Connecticut, CT, USA), carbon-coated (R. Schalek, and J. Lichtman, Harvard University, Cambridge, MA, USA) Kapton tape.<sup>41</sup> Sections on Kapton were assembled onto adhesive carbon tape (Science Services) attached to 4-inch silicon wafers (Siebert Wafer). Kapton and silicon were connected by adhesive carbon tape strips (Science Services) for grounding. EM micrographs were acquired on a Crossbeam Gemini 340 SEM (Zeiss) with a four-quadrant backscatter detector at 8 kV. In ATLAS5 Array Tomography (Fibics), the whole wafer area was scanned at 8000 nm per pixel to generate an overview map. In total, 130–160 sections were selected and imaged at  $200 \times 200 \times 200 \text{ nm}^3$  and a region at the dorsal spinal cord acquired at  $20 \times 20 \times 200 \text{ nm}^3$ . High-resolution micrographs ( $3 \times 3 \text{ nm}^2$ ) were taken from smaller regions on selected sections. The  $20 \times 20 \times 200 \text{ nm}^3$  image stacks were aligned by a sequence of automatic and manual processing steps in Fiji TrakEM2.<sup>36</sup> VAST software was used for reconstructions.<sup>42</sup> A region of  $150 \times 50 \mu\text{m}$ , at a  $50 \mu\text{m}$  distance from the middle dorsal vein, was used for quantification. The area of each numerated myelinated and unmyelinated axon was measured every  $2 \mu\text{m}$  (10 slices) throughout the stack (130–160 slices). Only axons that could be followed by at least 70 slices were included. Given that the difference between control and mouse NMO experiments was obvious, we relinquished scoring the morphological axonal changes blindly. Axonal diameter changes were scored as swellings, if the diameter locally increased by at least 50%. Swellings that could not be followed completely were excluded from the analysis. The number of swellings per axon was referred to the measured length of axon to get a longitudinal density.

### NMO survival surgeries

Mice were anaesthetized by intraperitoneal injection of fentanyl (0.05 mg/kg), Midazolam (5 mg/kg), Medetomidin (0.5 mg/kg) (MMF). Anaesthesia was reapplied when needed. After a double dorsal laminectomy over the L5 and L6 segments, the dura mater was punctured with the tip of a hypodermic needle to allow insertion of intrathecal catheter (ALZET® 0007743). The catheter was secured to surrounding tissues using 4–0 Ethilon sutures, and dorsal side was covered with 2% agarose in aCSF. Two additional punctures in the dura mater were made at the caudal end of the surgery site to avoid pressure increases during the superfusion. Recombinant antibodies rAQP4-IgG (7-5-53,  $6 \mu\text{g}/\text{ml}$ ) or rCtrl-IgG (ICOS-5-2,  $6 \mu\text{g}/\text{ml}$ ) with 20% of healthy donor serum, diluted in aCSF, were subdurally superfused for 90 min with a  $150 \mu\text{l}/\text{h}$  flow rate using a syringe pump. Afterwards, the catheter was removed and the surgical site was covered with 2% agarose in aCSF. The incision site was closed with wound clips, and mice were given post-surgery analgesia (Metacam, 2 mg/kg), followed by administration of Atipamezol (2.5 mg/kg), Flumazenil (0.5 mg/kg) and Naloxon (1.2 mg/kg) to antagonize MMF. 0.9% NaCl solution was delivered subcutaneously for rehydration. Animals were kept on heating pads until fully recovered. Mice were sacrificed on the next day via isoflurane overdose and transcardially perfused with  $1 \times \text{PBS}$  and 4% PFA. Tissues were fixed overnight with 4% PFA at  $4^\circ\text{C}$ . To define areas of substantial astrocyte depletion, whole mounts of fixed spinal cords up to 4–5 segments in length were prepared. Tissues were embedded in 1% agarose in  $1 \times \text{PBS}$ , with the dorsal surface facing a cover glass. These hanging drop preparations were scanned on an Olympus FV1000 confocal microscope with  $20 \times /0.8 \text{ NA}$  and  $60 \times /1.42 \text{ NA}$

oil-immersion objectives using z-steps of 1 and  $0.7 \mu\text{m}$ , respectively. High-resolution images taken with an  $60 \times /1.42 \text{ NA}$  objective were used for quantification. Only areas rostral to the surgical site were analysed to avoid any surgery-related injuries. In rAQP4-IgG treated mice, only astrocyte-depleted regions were included in the evaluation of axonal beading, which was performed blinded. Only axons observable for at least  $50 \mu\text{m}$  in length were included in the analysis.

### Image processing/representation

Images were processed using the open-source image analysis software Fiji and Adobe Creative Suite. For some figure representations, different channels of confocal image series were combined using pseudo-colour in Adobe Photoshop. In non-quantitative panels, gamma value was adjusted non-linearly to enhance visibility of low-intensity objects. Datasets were processed with Excel (Microsoft Corporation, Redmond, WA, USA).

### Data analysis

Results are presented as mean  $\pm$  SEM. Statistical significance was analysed with the GraphPad Prism 9 software using Mann-Whitney tests for comparing two groups and non-parametric ANOVA followed by Kruskal-Wallis tests for comparing more than two groups unless stated otherwise. P-values  $<0.05$  were considered to be significant, and are indicated with asterisks as follows: \* $P < 0.05$ ; \*\* $P < 0.01$ ; \*\*\* $P < 0.001$ .

### Data and material availability

All data are available in the main text or the [Supplementary material](#), unless indicated otherwise. Primary data tables will be made available by the authors on reasonable request. Mouse lines can be requested from the providing investigators and are protected by standard MTAs.

## Results

### Axonal beading occurs in early NMO lesions

We used biopsy and autopsy specimen of acute NMO lesions, where astrocyte loss, demyelination, immune infiltration and reduced axonal density have been previously described<sup>12</sup> to characterize NMO-related axonal pathology. For this, we identified seven early NMO lesions (five out of nine screened biopsies, two out of nine autopsies; [Table 1](#)) that contained MRP14-positive macrophages—a marker for early stage lesions<sup>34</sup>—and had suitable axon orientation to score axon injury as revealed by neurofilament stainings, while neurofilament stainings showed evidence of abundant axon swellings ([Fig. 1A](#)), tracing axons was difficult, however. Therefore, we used Bielschowsky impregnations ([Fig. 1B and C](#)) to further characterize axonal morphologies. Using this technique, a ‘pearls-on-string’ pattern of axonal beading was apparent in NMO lesions and greatly increased compared to perilesional white matter and control tissues (five biopsies/four autopsies of unrelated pathologies; for details, see [Table 2](#) and [Fig. 1B](#)). Previously, we had developed an *in vivo* two-photon imaging approach of the exposed mouse spinal cord, where topical AQP4-IgG/complement application induces almost complete loss of local subpial astrocytes in white matter tracts, which can also be used to study axonal pathology.<sup>28</sup> We therefore turned to this approach to directly study the dynamics and mechanisms underlying axon injury,<sup>24,25,43</sup> to better understand the emergence of axonal beading found in NMO lesions.

## Axonal beading precedes calcium dyshomeostasis in experimental NMO lesions

In many neuropathological settings, axonal pathology (such as spheroid formation) is preceded by calcium overload in the cytoplasm,<sup>44,45</sup> either derived from intracellular stores,<sup>46</sup> or from influx of extracellular calcium via ion channels<sup>47,48</sup> or non-specific membrane disruptions.<sup>25,32</sup> While sometimes reversible,<sup>32</sup> such calcium overload can cause activation of destructive intracellular signalling cascades that eventually result in irreversible axon degeneration.<sup>44</sup> Thus, we tested whether in our experimental NMO model, intra-axonal calcium elevation precedes axonal beading. We used *Thy1:TNXXL* transgenic mice, which express a fluorescence resonance energy transfer-based calcium sensor in neurons.<sup>31</sup> As in our previous experiments,<sup>28</sup> application of complement together with NMO patient-derived AQP4-IgG or recombinant (r) AQP4-IgG induced fast and progressive beading of many axons within a 6-h observation period (Fig. 1D and E and Supplementary Video 1; astrocyte survival for patient-derived AQP4-IgG at 3 h measured in *Aldh111:GFP × Thy1:OPFP3* mice, mean ± SEM: NMO 3.8 ± 2.5%, n = 6). Such axonal damage was largely absent after application of complement with IgG from healthy donor or recombinant control-IgG (Fig. 1D and E). In contrast to other models of neuroinflammation or trauma,<sup>24,32</sup> no axons progressed or recovered from beading during the imaging period, suggesting a relatively stable state of axon injury. Unexpectedly, we found that most beaded axons did not show an increase in calcium level during the first 6 h of astrocyte ablation (Fig. 1D and E). Moreover, the minority of axons in which calcium increases showed this increase with substantial delay, and no axon showed a detectable calcium increase before axonal beading started (Fig. 1F). Also, there was no fixed temporal relationship between the onset of axonal beading and of the calcium rise (Fig. 1G). Altogether, these data indicate that AQP4-IgG mediated astrocyte loss induces a distinct form of axon pathology, which is calcium-independent at onset and only inconsistently leads to subsequent impairment of axonal calcium homeostasis. This cascade thus reverses the sequence of events found in previously described forms of axonal injury,<sup>44,45</sup> including neuroinflammation.<sup>25,47</sup>

## Experimental NMO lesions lead to persistent axonal beading

We next explored whether beading was a transient or lasting pathology. As acute *in vivo* two-photon imaging only allowed us to follow early axonal injury within a 6-h time window, we turned to a survival surgery approach to assay chronic axonal changes after initiation of experimental NMO lesions<sup>32,49</sup> (Fig. 2). For this, we exposed the dorsal spinal cords of *Aldh111:GFP × Thy1:OPFP3* mice to rAQP4- or rCtrl-IgG plus human complement. One day after surgical closure of the laminectomy, the animals were perfused and the spinal cords were examined by confocal microscopy (for details, see Methods). Application of rAQP4-IgG, compared to rCtrl-IgG, induced a pronounced reduction in astrocyte density in many areas of the spinal cord (Fig. 2A and B). Analysis of axonal beading showed that while a subset of axons also had calibre variations in rCtrl-IgG-treated spinal cords (most probably due to the opening of the dura required for IgG application), astrocyte ablation by AQP4-IgG induced a significantly higher fraction of beaded axons (Fig. 2C), suggesting that NMO-related axonal beading is a persistent phenomenon. We did not observe any axon fragments, which typically last for days in the spinal cord,<sup>49</sup> suggesting

that axonal beading represents a stable dysmorphic state that can persist for days.

## Beading predominantly affects small calibre axons independently of myelination

In addition to astrocyte loss, demyelination is another hallmark of NMO lesion pathology.<sup>50,51</sup> Axonal beading could be the immediate consequence of myelin pathology.<sup>52</sup> This would predict that only myelinated axons would undergo beading after AQP4-IgG induced astrocyte loss. As myelination requires a target axon above a threshold diameter,<sup>53,54</sup> large calibre axons would be expected to be most vulnerable to beading. However, when we compared the axon calibre of the beaded versus the non-beaded axons in *Thy1:TNXXL* mice, thinner axons were actually more vulnerable to beading (Fig. 3A). Based on this observation, we assumed that unmyelinated axons might also develop beading due to astrocyte loss. Given the resolution limitations of light microscopy and hence its ability to differentiate between myelinated and unmyelinated axons in dense white matter tracts, we examined the morphology of myelinated and unmyelinated axons in mouse NMO lesions via serial section EM (Fig. 3B–E and Supplementary Video 2). This approach revealed that in addition to myelinated axons, also unmyelinated axons showed the beading phenomenon (mean ± SEM: NMO  $n_{myel} = 47.4 \pm 10.4\%$ ,  $n_{unmyel} = 74.1 \pm 4.4\%$ ; n = 3 mice; Fig. 3E). Notably, also control unmyelinated axons showed calibre variations (mean ± SEM: control  $n_{unmyel} = 30.5 \pm 11.3\%$ ; n = 3 mice), which can probably be explained by pre-synaptic varicosities,<sup>55</sup> but the beading phenomenon could be clearly identified by a significant increase in swelling density induced in the experimental NMO lesions (mean ± SEM: control  $0.046 \pm 0.00$  versus NMO  $0.065 \pm 0.003$  swellings/ $\mu\text{m}$ ; Mann–Whitney test, \*\*\*P < 0.001). Overall, the axonal injury following AQP4-IgG mediated astrocyte loss especially affects thin axons, whether they are myelinated or not, and therefore it is unlikely to be initiated by NMO-related myelin pathology.

## Axonal beading involves local cytoskeletal remodelling driven by osmo-ionic overload

Another potential driver of axon shape changes is cytoskeletal remodelling, which in some cases can, for example, result in local organelle accumulations due to disrupted transport.<sup>44,56</sup> We used transmission EM to directly assess the cytoskeleton inside beaded axons and found that microtubules were unusually sparse and disorganized, in contrast to the well-organized cytoskeletal structures in control axons (Fig. 4A). In line with these ultrastructural results, confocal analysis of tubulin immunostainings (Fig. 4B and C) revealed local loss and reorganization of microtubules at the centre of axonal beads compared to well-preserved parallel-running microtubule bundles outside the swellings or in control axons (Fig. 4B). We quantified  $\beta$ III-tubulin immunofluorescence relative to a fluorescent protein (OPFP) transgenically expressed in axons. Tubulin staining was reduced by >50% within axonal beads either compared to the interjacent axon segments in AQP4-IgG-induced lesions, or to axons under control conditions (Fig. 4C). As cytoskeletal breakdown is known to occur during Wallerian degeneration and related processes,<sup>56,57</sup> we explored whether deleting a central mediator of Wallerian-like degeneration, sterile alpha and TIR motif-containing protein 1 (SARM1)<sup>58</sup> would affect NMO-related axon beading. In SARM1-deficient mice, treatment with AQP4-IgG/complement resulted in similar kinetics and extent of

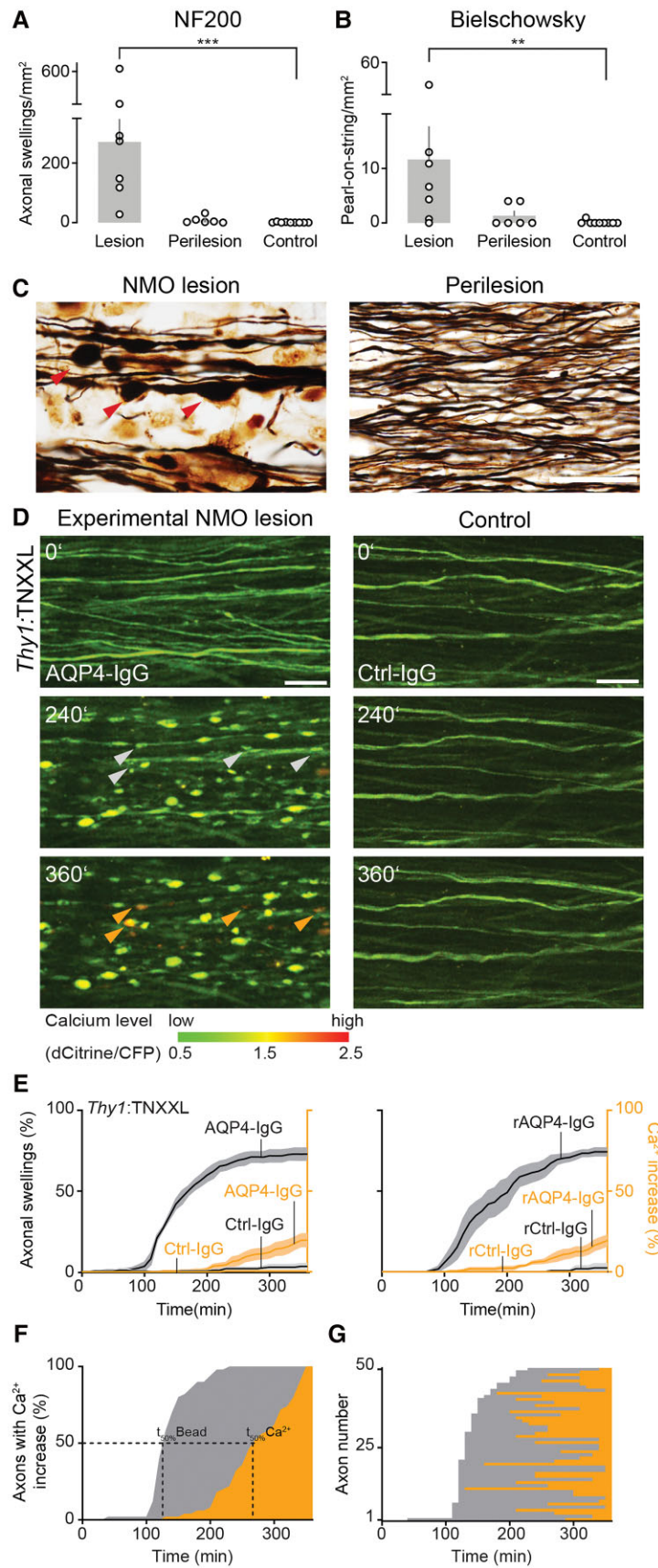


Figure 1 Axonal beading occurs in NMO lesions and precedes calcium rise. (A) Density of beaded axons quantified in NF200 (Continued)

axon loss as in heterozygote *SARM1*<sup>+/-</sup> mice (fraction of surviving astrocytes after 3 h, mean ± SEM: *SARM1*<sup>-/-</sup>: 2.3 ± 1.9%; *SARM1*<sup>+/-</sup>: 2.4 ± 1.4%, *n* = 5 mice each), without a difference in the degree of axonal beading (Fig. 4D). Thus, Wallerian-like degeneration does not appear to play a key role in NMO-related axon injury. Moreover, it is known that also non-Wallerian caspase-dependent pathways can contribute to axon degeneration in the spinal cord.<sup>59,60</sup> Therefore, we tested a pan-caspase inhibitor, zVAD (200 μM) during AQP4-IgG lesion induction *in vivo*. Pretreatment (for 60 min) and following continuous application of zVAD during AQP4-IgG lesion induction did not show any difference in axonal beading formation or calcium rise (data not shown). Thus, a caspase-dependent mechanism of axonal degeneration is unlikely to be the mediator of the observed axonal pathology.

Another notable ultrastructural feature of the axonal beads was that they typically showed few membranous organelles, in contrast to axonal swellings that result from ‘traffic jams’ of organelle transport.<sup>61</sup> As this scarcity in organellar content could indicate cytoplasmic expansion due to cellular oedema, and because astrocytes via AQP4 play a central role in water homeostasis,<sup>62</sup> we probed whether changing the osmotic milieu by applying a hyperosmolar (200% of the initial osmolarity) mannitol solution would affect acute axonal beading. Indeed, this delayed and significantly reduced the number of beaded axons during experimental NMO lesion formation (Fig. 4E). At the same time, astrocytes were still efficiently ablated by AQP4-IgG/complement treatment (fraction of surviving astrocytes after 3 h, mean ± SEM: 1.5 ± 0.5%, *n* = 4). Similarly, reducing the sodium influx to axons using the voltage-gated sodium channel blocker tetrodotoxin (TTX, 1 μM) also significantly protected axons from beading (Fig. 4F), while astrocytes were still lysed (fraction of surviving astrocytes after 3 h, mean ± SEM: 3.0 ± 2.3%, *n* = 6).

If the iono-osmotic imbalance is responsible for the observed axonal beading, an ablation of astrocytes in combination with osmolarity changes should be sufficient to provoke axonal beading. To test this, we applied a pro-apoptotic drug, HA-14, which ablates astrocytes over a similar time span, albeit less extensively compared to AQP4-IgG/complement treatment (astrocyte survival after 3 h, mean ± SEM: 29.2 ± 2.6%, *n* = 4; Fig. 4G). After 3 h, we decreased the osmolarity of aCSF by 10% (via dilution with H<sub>2</sub>O). The reduced astrocyte density combined with this mild hypo-osmolar milieu led to axonal beading in a similar pattern as in our NMO model (axonal beading in % at 190 min, mean ± SEM: 12.8 ± 2.4, *n* = 3; control DMSO: 2.2 ± 0.2%, *n* = 3; Fig. 4G).

Similarly, destabilizing microtubules combined with hypo-osmolarity should also induce beading at least transiently. We thus applied the microtubule destabilizing drug Nocodazole,

which alone did not induce axonal beading, although this treatment efficiently destabilized microtubules as shown by tubulin-βIII staining (Fig. 4H). However, the combination of Nocodazole with mild hypo-osmolarity again induced axonal beading (axonal swelling in % at 190 min: 11.9 ± 3.0%, *n* = 5), that was absent under control condition (Fig. 4H DMSO, replot from 4G).

Altogether, these results imply that osmotic and ionic overload, probably due to astrocyte necrosis, together with calcium-independent cytoskeletal remodelling mediate the initial phase of acute axonal beading in our NMO model.

### Microtubule stabilization prevents acute axonal beading in experimental NMO lesions

While microtubule loss is not an early or dominant feature in multiple sclerosis-related forms of axon degeneration,<sup>63</sup> in some traumatic and neurodegenerative settings,<sup>29,64</sup> microtubule alterations are prominent in injured axons and might also contribute to the intrinsic inefficiency of CNS axon regeneration. Accordingly, microtubule stabilization using taxenes or related drugs<sup>29,65</sup> has been explored as pro-regenerative intervention after axon transection. Whether such an approach could be used for axon protection in NMO-related pathology is unknown.

We therefore explored this approach in our NMO model. Indeed, local application of the microtubule stabilizer epothilone B (epoB) during AQP4-IgG/complement treatment, greatly reduced the number of beaded axons, while it did not affect astrocyte survival (Fig. 5A–C). Similarly, as epoB is CNS-permeant, intraperitoneal injection of epoB<sup>29</sup> 24 h before local lesion induction also reduced axonal beading (Fig. 5D). Analysis of βIII-tubulin immunostainings confirmed microtubule stabilization after local epoB treatment, as microtubule content was significantly preserved in axon beads (Fig. 5E), but also in interjacent non-beaded axon segments (βIII-tub/OPF ratio after epoB: 1.66 ± 0.17, *n* = 65 axons versus vehicle: 0.57 ± 0.05, *n* = 188, 5 mice each). Overall, these results imply that microtubule stabilization might be a suitable strategy to protect axons during early phases of NMO lesion formation that could be explored in suitable chronic NMO models.

## Discussion

Astrocyte pathology—the structural hallmark of NMO—has been implicated in neuronal dystrophy associated with many neurodegenerative and neuroinflammatory diseases.<sup>16,66,67</sup> So far, these observations have been largely confined to the chronic phases of lesion formation and involved the slow development of reactive astrocyte phenotypes.<sup>21,27</sup> Often, the impact of such a neurotoxic

### Figure 1 Continued

staining and (B) Bielschowsky silver impregnations. NMO lesions (beaded axons/μm<sup>2</sup>: Bielschowsky: 11.7 ± 6.0, NF200: 271.1 ± 75.6; *n* = 7 patients), perilesion (Bielschowsky: 1.3 ± 0.8, NF200: 8.3 ± 4.9; *n* = 6), control white matter (Bielschowsky: 0.1 ± 0.1, NF200: 0.7 ± 0.5; *n* = 9). Data represent mean ± SEM; NMO lesions versus control \*\**P* = 0.004 (left), \*\*\**P* = 0.0002 (right); Kruskal–Wallis test followed by Dunn’s multiple comparisons test. (C) Representative ‘pearls-on-string’ axonal beading (red arrowheads) morphology in a Bielschowsky silver impregnation of an early NMO lesion (left). Very few beading were observed in perilesional white matter (right). Scale bar = 20 μm. (D) *In vivo* two-photon time-lapse imaging showing development of axonal beadings (white arrowheads) and intracellular calcium rise (orange arrowheads) at the indicated times (minutes) after AQP4-Ig/complement application. Axons remain unaffected in control experiments (Ctrl-IgG/complement). Calcium levels pseudo-colour coded as indicated; scale bar = 20 μm. (E) Increase of beaded (grey) and high-calcium-containing axons (orange) in *Thy1:TNXXL* mice over 6 h after experimental NMO lesion induction. The majority of labelled axons showed beading (NMO left: AQP4-IgG: 73.0 ± 3.7%, *n* = 5 mice; rAQP4-IgG: 74.3 ± 2.4%, *n* = 4; versus control right: Ctrl-IgG: 3.4 ± 1.7%, *n* = 4; rCtrl-IgG: 2.5 ± 2.5%, *n* = 3), Mann–Whitney test, \**P* (AQP4-IgG versus Ctrl-IgG) = 0.015, in some followed by calcium rise (threshold: dCitrine/CFP ≥ 1.5; NMO left, red graph: AQP4-IgG: 19.6 ± 3.9%; rAQP4-IgG: 19.4 ± 3.1% versus control Ctrl-IgG: 0.5 ± 0.5%; rCtrl-IgG: 0 ± 0%). Data represent mean ± SEM. *n* > 200 axons were analysed for each condition. (F) Population and (G) individual axon data (ordered by time of beading onset) showing the relative time course of beading (grey) and calcium elevation (orange) in the subset of axons that lost calcium homeostasis. While on average, the calcium rise was delayed by 136 ± 9 min [*t*<sub>50%</sub>(beading) – *t*<sub>50%</sub>(calcium rise); mean ± SEM], on an axon-to-axon level, there was no consistent temporal relationship between the time of beading and of calcium rise. *n* = 50 high-calcium axons from five experiments.



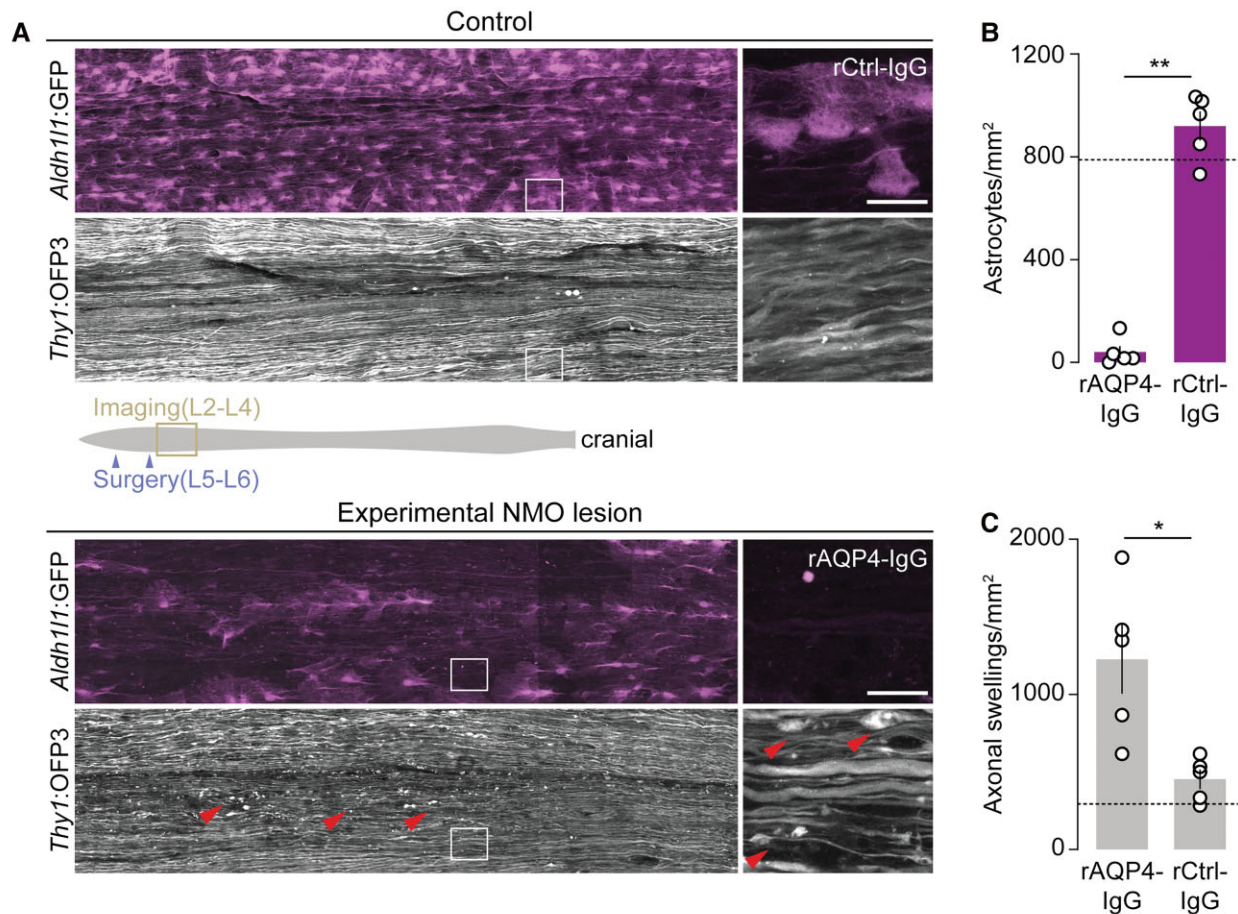


**Figure 2** Astrocyte depletion leads to persistent axonal beading in experimental NMO lesions. (A) Representative overview confocal images of spinal cord whole mounts of *Aldh11:GFP* × *Thy1:OFP3* mice. In control tissue (top), astrocytes (*Aldh11:GFP*, magenta) remained mostly unaffected 24 h after superfusion with rCtrl-IgG/complement (90 min) with only a small number of axons showing swellings (*Thy1:OFP3*, grey), possibly due to surgery. In experimental NMO lesions 24 h after superfusion with rAQP4-IgG/complement (for 90 min; bottom), astrocyte loss and axonal beadings (arrowheads) were apparent. Note patchy astrocyte loss probably due to the non-homogenous distribution of rAQP4-IgG/complement in subdural space; only substantially astrocyte-depleted areas were included in analysis. (B) Astrocyte density within analysed areas of chronic lesions and control-treated spinal tissue (rCtrl-IgG:  $920 \pm 57$  versus rAQP4-IgG:  $40 \pm 24$  mm<sup>-2</sup>,  $n = 5$  mice each). (C) Density of beaded axons in experimental NMO lesions versus control-treated spinal tissue (rCtrl-IgG:  $453 \pm 63$  versus rAQP4-IgG:  $1227 \pm 222$  mm<sup>-2</sup>,  $n = 5$  mice each). Only astrocyte-depleted regions were included in the analysis for the rAQP4-IgG group. Dashed lines indicate the average density of astrocytes (B) and swollen axons (C) quantified in mice without any surgical interventions ( $n = 3$  mice). Schematic representation of spinal cord (grey) with surgery (purple arrowheads) and imaging (yellow box) areas is shown in A. Boxed areas are magnified on the right.  $n \geq 48$  axons were analysed per animal. Data are represented as mean  $\pm$  SEM. Mann-Whitney test; \*\* $P = 0.0079$  in B; \* $P = 0.0159$  in C. Scale bars = 40  $\mu$ m.

polarization of astrocytes is mediated via indirect cellular signalling involving microglial crosstalk, e.g. in models of multiple sclerosis,<sup>16,17</sup> a mechanism recently also implicated in chronic NMO lesions.<sup>68</sup> In contrast, the impact of acute astrocytic injury during the early phases of NMO lesion formation has received less attention, even though the swift development of lasting axonal injury and persistent neurological deficits are characteristic of this neuroinflammatory disease.<sup>11</sup> Understanding the underlying axon injury mechanisms is important, as in contrast to more common neuroinflammatory diseases—such as multiple sclerosis—the first episode of NMO often already has devastating consequences that would need acute neuroprotective intervention, in addition to ameliorating relapse risk by subsequent immunomodulatory intervention.<sup>69</sup>

Here we describe ‘acute axonal beading’ as the swift consequence of *in vivo* astrocyte loss and as the earliest observable axon injury in acute experimental NMO lesions. Acute axonal beading represents a

new form of calcium-independent axonal pathology that is distinct from the mechanisms of axon injury previously described during multiple sclerosis-related neuroinflammation or trauma. We show that after lytic depletion of astrocytes, axonal microtubules are reorganized and diminished, accompanied by fast and lasting axon beading in a ‘pearls-on-string’ pattern that is evident in NMO lesions as well (Fig. 1C). These insights regarding the mechanisms of axon loss<sup>70,71</sup> are important, as they hint towards cytoskeletal stabilization as a possible intervention point for acute neuroprotection during destructive episodes of NMO, but make other interventions targeting processes such as Wallerian-like degeneration, appear less promising.

Acute axonal beading has characteristics that set it apart from other pathways that hitherto have been implicated in axon pathology in general, and especially in axonal spheroid formation.<sup>56</sup> One central feature that is distinct in NMO-related acute axonal beading compared to most previously proposed axon injury

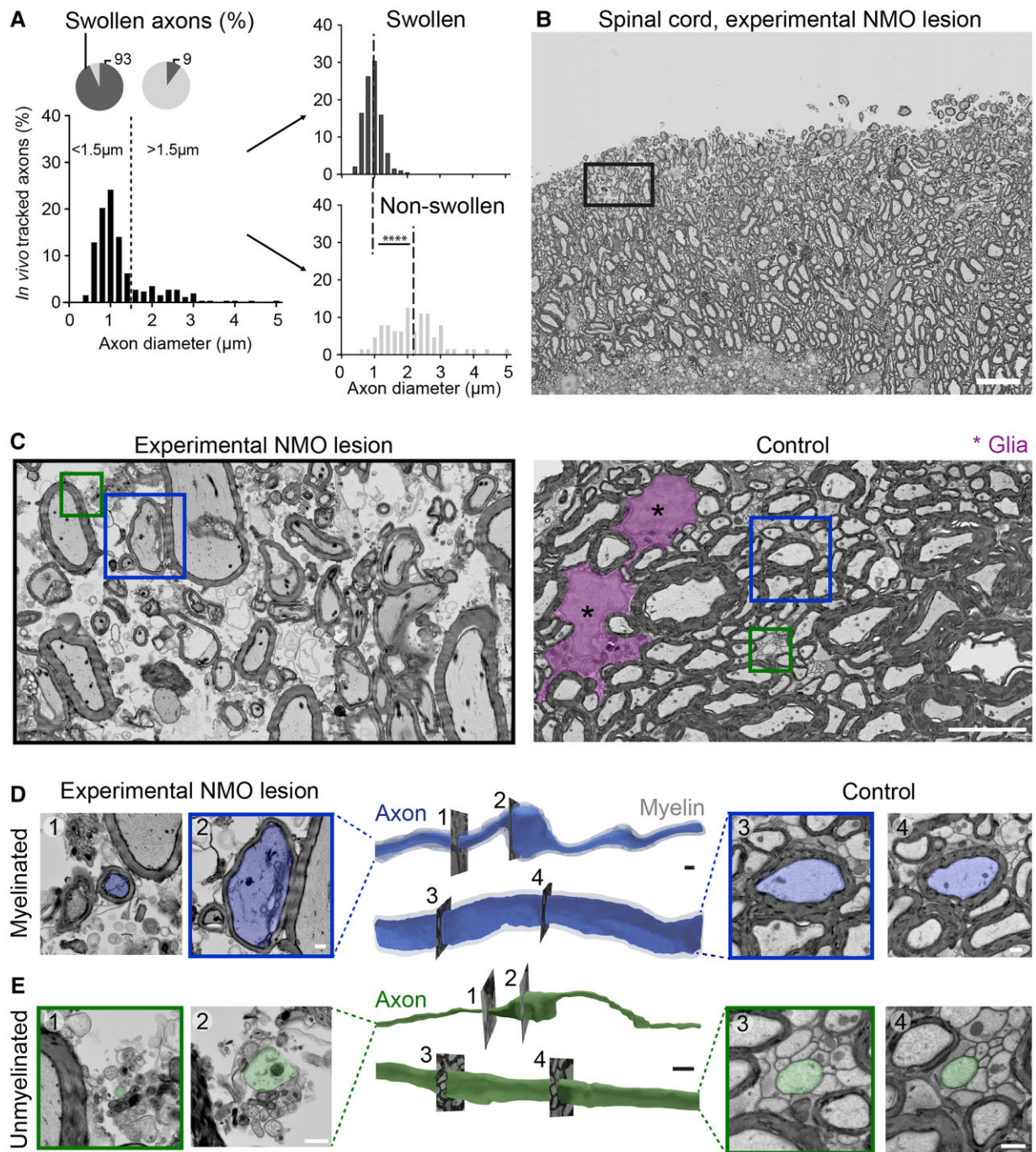


**Figure 3** Electron microscopy analysis of axonal pathology in experimental NMO lesions. (A) Histograms of axon calibre distribution of the axon population imaged *in vivo* in Thy1:TNXXL mice (>250 axons from  $n=5$  mice, binning  $0.2\ \mu\text{m}$ ). Overall population (left) and split into swollen/non-swollen (right) after 6 h of AQP4-IgG/complement application. Pie charts: thin axons were more likely to swell (< $1.5\ \mu\text{m}$ :  $93 \pm 1.7\%$  versus > $1.5\ \mu\text{m}$ :  $9.1 \pm 3.2\%$ ;  $n=5$  mice). Dotted dashed lines in right diagrams represents mean of initial diameter in swollen and non-swollen axon populations. Data represent mean  $\pm$  SEM. Mann-Whitney test, \*\*\*\* $P < 0.0001$ . (B and C) Volume EM analysis by tape-based scanning EM of mouse spinal lesions 6 h after NMO induction (resolution:  $20 \times 20 \times 200\ \text{nm}^3$ ). (B) Cross-section image of dorsal spinal column. Boxed area: xy position of the 3D data series used in C. Scale bar =  $20\ \mu\text{m}$ . Higher magnification images of experimental NMO lesion (C, left) shows oedema, glial cell loss and axonal injury. In control tissue (right), tightly packed axons and glial cells (magenta) were visible without signs of oedema or cell loss. Boxes: Axons analysed in D and E. Scale bar =  $5\ \mu\text{m}$ . (D and E) 3D surface rendering of myelinated (D; axon: blue, myelin: grey) and unmyelinated axons (E; green). Representative cross-sections of non-swollen (1) and swollen (2) axon segments in experimental NMO lesion (left) and of non-swollen axons with comparable diameters (3, 4) in control conditions (right). Scale bar =  $1\ \mu\text{m}$ .

cascades is the lack of initial calcium overload; indeed, in our observations, axonal beading was typically complete before signs of calcium overload appeared without any evident fixed time delay

(range of delay: 10 to 250 min; Fig 1F and G). In contrast, most other forms of axon injury show signs of calcium dysregulation before structural axon pathology becomes apparent, including multiple

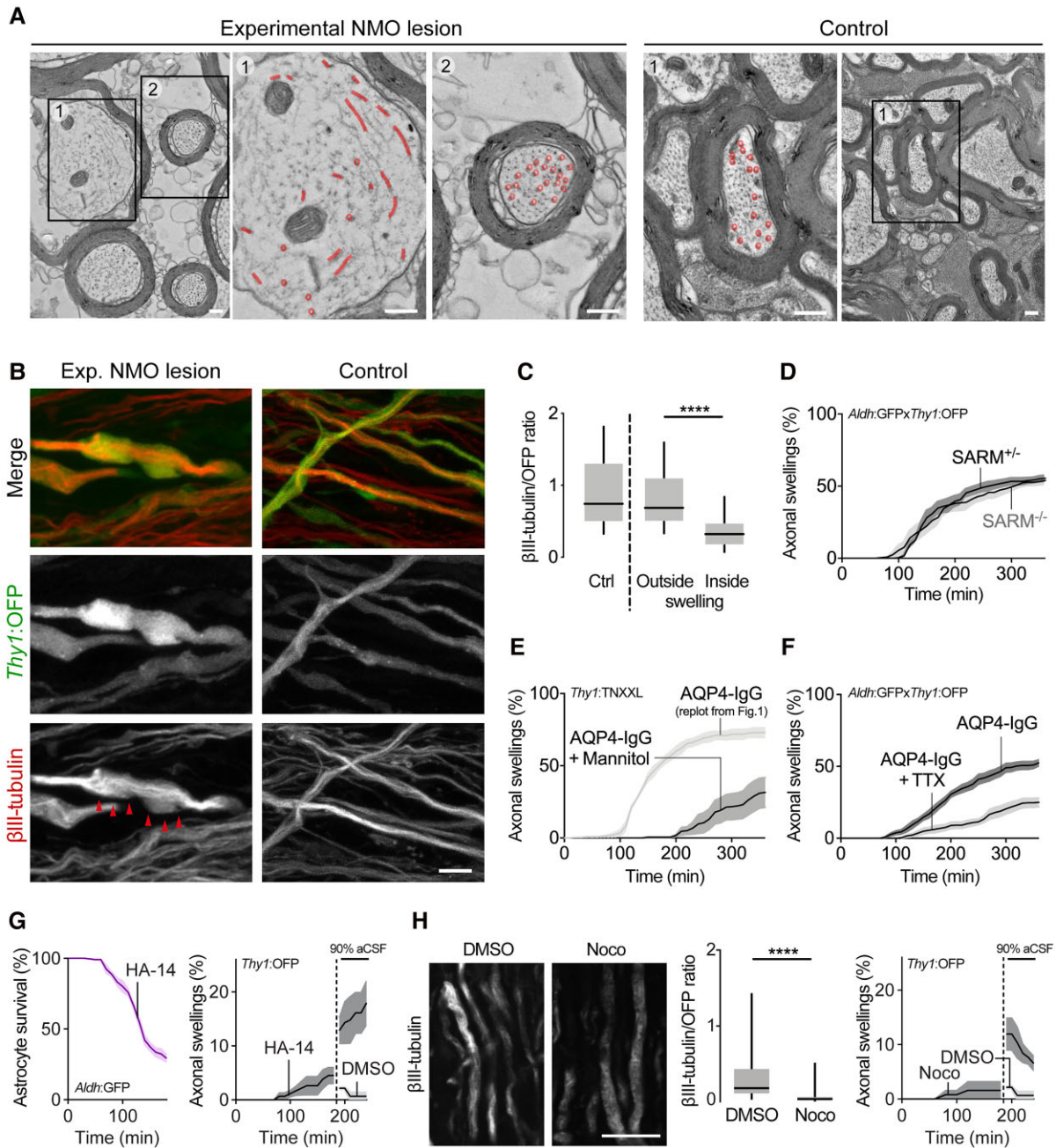


**Figure 4** Axonal beadings show cytoskeletal disruptions, driven by ionic- and osmotic overload. (A) High-resolution transmission EM analysis of swollen axons in an experimental NMO lesion shows oedema and microtubule disorganization (red) within beadings (left, 1). Well-arranged, densely packed microtubules (red) are visible in neighbouring non-swollen axon areas (2) and in control tissue (right, 1). Scale bar = 200 nm. (B) Confocal image of Thy1:OPF3 spinal cord axons (green), stained with  $\beta$ III-tubulin antibody (red) after 6 h application of AQP4-IgG or Ctrl-IgG/complement. Red arrowheads point to an axon bead containing disorganized microtubules. Scale bar = 5  $\mu$ m. (C) Quantification of  $\beta$ III-tubulin mean fluorescent intensity (MFI) normalized to OPF signal of Thy1:OPF3 axons in control tissue (median: 0.75,  $n = 137$  axons) and experimental NMO lesions (median, outside: 0.69; inside: 0.32,  $n = 102$  axons;  $n = 5$  mice for each condition). Box-and-whisker plot: 10–90 percentile. Kruskal–Wallis test followed by Dunn’s multiple comparisons test using axons, \*\*\* $P < 0.0001$ . (D) Percentage of swollen axons within 6 h of experimental NMO lesion induction was similar in SARM1-deficient KO versus heterozygous mice in *Aldh1l1:GFP*  $\times$  *Thy1:OPF3* background (*SARM1*<sup>-/-</sup>: 54.0  $\pm$  3.1%; *SARM1*<sup>+/-</sup>: 55.5  $\pm$  2.7%; from  $n = 5$  mice each), as well as to wild-type *Thy1:OPF3* mice (cf. F). (E) Local application of hyperosmolar (200% of the initial osmolarity) mannitol solution delayed and diminished beading in NMO spinal lesions (mean  $\pm$  SEM: 31.5  $\pm$  10.4%,  $n = 5$  *Thy1:TNXXL* mice). Percentage of swollen axons induced by AQP4-IgG/complement under normal osmotic conditions from Fig. 1 replotted for comparison (73.0  $\pm$  3.7%,  $n = 5$ ). Mann–Whitney test, \*\* $P = 0.0079$ . (F) Local treatment with voltage-gated sodium channel blocker TTX (1  $\mu$ M) reduced the number of swollen axons (*SARM1*<sup>-/-</sup>: 52.4  $\pm$  2.4%;  $n = 6$  *Aldh1l1:GFP*  $\times$  *Thy1:OPF3* mice for each condition). Mann–Whitney test, \*\* $P = 0.0022$ . (G) Astrocyte depletion via application of the pro-apoptotic drug, HA-14 (left, astrocyte survival after 3 h, mean  $\pm$  SEM: 29.2  $\pm$  2.6%,  $n = 4$ ) induced sensitivity of axons to develop beadings following a mild hypo-osmotic change (90% aCSF; right, at 190 min, mean  $\pm$  SEM: 12.8  $\pm$  2.4%,  $n = 3$ ; control DMSO: 2.2  $\pm$  0.2%,  $n = 3$ ; Mann–Whitney test,  $P = 0.1$ ). (H) Quantification of  $\beta$ III-tubulin in spinal tissue following the local treatment with microtubule destabilizing drug Nocodazole. Scale bar 10  $\mu$ m.  $\beta$ III-tubulin MFI normalized to OPF signal of *Thy1:OPF3* axons in control (DMSO, median: 0.18,  $n = 100$  axons,  $n = 2$  mice) and Nocodazole treated mice (Noco, median: 0.04,  $n = 99$  axons,  $n = 2$  mice). Box-and-whisker plot: min to max. Mann–Whitney test, \*\*\*\* $P < 0.0001$  (middle). Microtubule destabilization induced axonal beadings under hypo-osmolar condition (right, at 190 min; Noco: 11.9  $\pm$  3.0%,  $n = 5$ ; DMSO 2.2  $\pm$  0.2%,  $n = 3$ ; Mann–Whitney test, \* $P = 0.0179$ ).

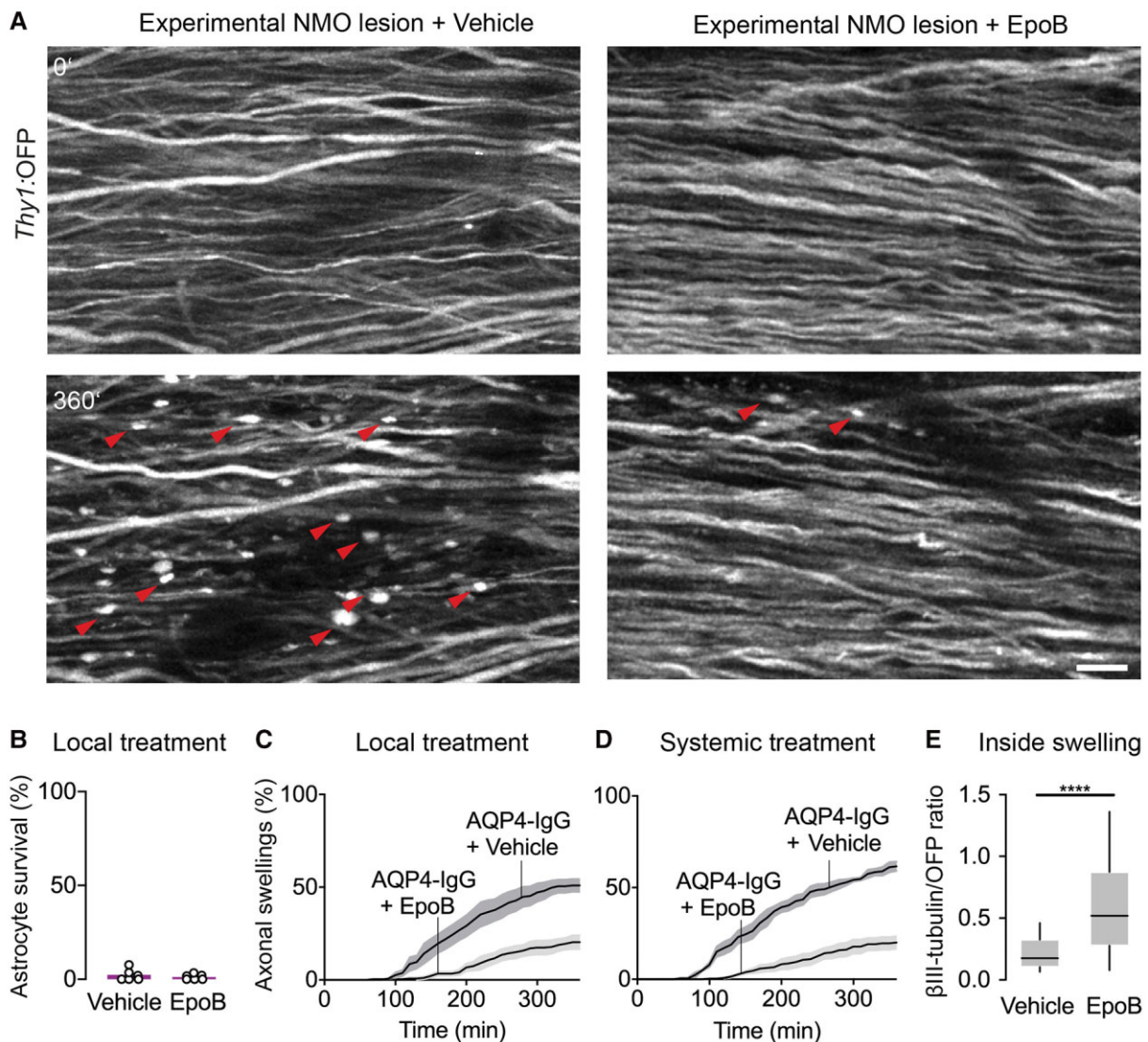


**Figure 5** Microtubule stabilization protects axons from beading. (A) *In vivo* two-photon imaging of *Aldh1l1:GFP* × *Thy1:OFP* mice spinal cord axons with-in 6 h of experimental NMO lesion induction with local epoB (5  $\mu$ g/ml) or vehicle application. Red arrowheads indicate axonal beading, which is diminished with epoB treatment. Scale bar = 20  $\mu$ m. (B) Unchanged depletion of spinal cord astrocytes following local epoB or vehicle treatment (survival after 3 h, epoB:  $2.3 \pm 1.3\%$  versus vehicle:  $1.2 \pm 0.6\%$ ;  $n = 6$  mice each). (C) Quantification of axonal beading after 6 h local epoB treatment (epoB:  $19.9 \pm 3.1\%$ ; vehicle:  $50.9 \pm 3.8\%$ ,  $n = 6$  mice each). Mann–Whitney test,  $P < 0.01$ . (D) The fraction of beaded axons was reduced following systemic administration of epoB 24 h before lesion induction (after 6 h:  $19.2 \pm 3.4\%$  versus vehicle:  $61.6 \pm 2.5\%$ ,  $n = 5, 4$  mice, respectively) Mann–Whitney test;  $P < 0.05$ . (E) Quantification of  $\beta$ III-tubulin staining mean fluorescent intensity (MFI) normalized to OFP signal in *Thy1:OFP* mice. Local epoB treatment preserved tubulin staining compared to vehicle (median, vehicle: 0.17 versus epoB: 0.52,  $n = 188, 65$  axons respectively in five mice each). Mann–Whitney test; \*\*\*\* $P < 0.0001$ . Box-and-whisker plot: 10–90 percentile. Data represent mean  $\pm$  SEM in B–D.

sclerosis-related neuroinflammation,<sup>25,72</sup> trauma<sup>32,73,74</sup> or hypoxia.<sup>75,76</sup> These cascades are initiated by the spurious leakiness of the membrane or calcium channels,<sup>77</sup> release from internal stores<sup>46</sup> or the reversal of calcium-carrying membrane pumps,<sup>78</sup> often as a consequence of sodium overload. In contrast, the axons in acute experimental NMO lesions do not seem to experience early calcium overload (Fig. 1E), even though TTX-sensitive voltage-gated sodium channels that act upstream of calcium in a range of axonal pathologies,<sup>79,80</sup> appear relevant for the beading process (Fig. 4F). However, this role probably relates more to a sodium influx-related osmotic challenge than to driving secondary calcium influx (see next). Similarly, mitochondrial dysfunction is an early hallmark of many pathways that involve ‘virtual hypoxia’ induced by ionic

overload and calcium dyshomeostasis.<sup>81</sup> However, our ultrastructural analysis did not show the characteristic mitochondrial pathology that can be found early, e.g. in many neurodegenerative conditions, in MS<sup>24,82</sup> or chronic NMO lesions.<sup>27</sup> Finally given its swift time course, the early axon pathology that we describe probably precedes infiltrating immune cells, as confirmed by histopathology and immunohistochemical stainings for different immune cell populations (data not shown).

The absence of early calcium influx also rules out a number of additional pathways of axon injury that have been suggested to drive neuroinflammatory axon loss. For instance, there could be a spurious attack by complement components that preassemble on astrocytes as part of the AQP4-mediated injury and spill over to

nearby axonal membranes. Such ‘bystander injury’ has been invoked to explain the spread of cellular injuries in NMO in general,<sup>83</sup> but also to neurons in particular.<sup>22</sup> However, whether such a mechanism could also affect axons in white matter tracts directly is unknown.<sup>84</sup> Our *in vivo* imaging data provide little support for this: The affected axons are mostly—albeit not all—myelinated, which would probably hinder access of a macromolecular attack complex such as complement,<sup>85</sup> except at the nodes of Ranvier. However, we see little evidence for an onset of beading at nodes, in contrast to swellings that we previously described in a model of multiple sclerosis.<sup>24</sup> Moreover, from previous work involving *in vivo* dye loading and calcium imaging,<sup>25,32</sup> we know that *in vivo* calcium imaging is sensitive to the presence of 10 nm pores, as would be expected if the MAC assembled on axonal membranes.<sup>85</sup> Thus, the late occurrence of calcium influx largely rules out the mechanisms of axonal bystander injury. Additionally, the non-lytic ablation of astrocytes (Fig. 4G) or, downstream, the direct destabilization of microtubules (Fig. 4H) sensitizes axons for beading induced by a mild hypo-osmotic challenge and thus recapitulates the findings in our experimental NMO model, without the presence of complement. Similarly to bystander injury, our experiments also do not provide evidence for formation of membrane nanoruptures,<sup>25</sup> as observed during another well-established inflammatory axon degeneration pathway, focal axonal degeneration, which is characteristic of multiple sclerosis,<sup>24,25</sup> but has also been implicated in chronic NMO.<sup>27</sup> Finally, Wallerian-like degeneration, which is the best understood molecular cascade resulting in axon swelling and subsequent fragmentation,<sup>49,56,86</sup> also typically involves calcium influx.<sup>23,87</sup> In line with the absence of such calcium influx, deletion of SARM—the central endogenous mediator of Wallerian degeneration<sup>58</sup>—had no discernible effect on NMO-related lesions (Fig. 4D). Thus, our data suggest that an axon injury pathway distinct from those previously described in neuroinflammation and trauma underlies acute axonal beading induced by astrocyte lysis in NMO. However, Wallerian degeneration at later time points (for instance, after several days) cannot be ruled out. It is possible that, for example, due to a transport deficit at later stages, the stable dysmorphic state of axonal beading progresses to a degenerative one. It is also conceivable that the microtubule changes observed here could represent a metastable condition that can later revert back to a more normal cytoskeleton. However, compared to other settings where we observed such transient axonal injury,<sup>24,25,32</sup> the changes induced by an NMO-related lesion seem to be more lasting, as no spontaneous reversals were apparent during the first 6 h after astrocyte loss. Still, definitive exploration to the chronic fate of beaded axons will require analysis in a suitable chronic model of NMO that is accessible to dynamic observation.

Despite these limitations for long-term observation, our intravital, ultrastructural and histological investigations reveal important acute features of this unusual form of axonal pathology: (i) while many axons ( $76 \pm 2.8\%$  in the dorsal column of *Thy1:TNXXL* mice; Fig. 3A and B) undergo beading, thin-calibre axons are especially vulnerable (Fig. 3A); (ii) this vulnerability does not strictly relate to myelination, as both myelinated and non-myelinated axons appear beaded in EM (Fig. 3D and E), making a geometrical or mechanical cause for the vulnerability of thin axons more likely; and (iii) the axonal beads show a striking reorganization of the cytoskeleton with local loss of microtubules (Fig. 4B). Together, this supports the view that cytoskeletal reorganization drives acute axonal beading, which further distinguishes NMO-related axon injury from other forms of inflammatory axon damage (cf. Sorbara et al.<sup>63</sup>).

The fact that acute axonal beading can be substantially ameliorated by stabilizing microtubules (Fig. 5), but also by blunting hypo-osmotic impact (Fig. 4E), corroborates this notion and points to a possible therapeutic target. Notably, the morphological and mechanistic features of NMO-related *in vivo* axon injury harbour parallels to a previously characterized *ex vivo* phenomenon of axonal beading, which is prominent in fixed and isolated PNS axons after stretch,<sup>88</sup> but can also be modelled *in vitro* using PNS axons exposed to osmotic shock.<sup>89</sup> Indeed, also in the *ex vivo* PNS stretch model, calcium was not required, myelinated, as well as non-myelinated axons were affected and local cytoskeletal changes were observed.<sup>88,90</sup> *In vitro*, axoplasm-filled swellings were described that had a microtubular ‘core’ strikingly similar to the microtubular arrangements we observed in NMO-related injury (cf. Fig. 2 in Datar et al.<sup>91</sup> with our Fig. 4B). A modelling analysis of the beading transformation<sup>91</sup> *in vitro* revealed that hyperosmotic shock disrupts the interplay of longitudinally running microtubules, sub-membranous actin and membrane surfaces tension resulting in a surface tension-driven shape destabilization that finally results in beading—again in line with our result that small calibre (and hence high surface-to-volume ratio) axons showed special vulnerability.

Targeting the microtubular cytoskeleton (e.g. by pharmacological stabilization using taxenes or epothilones<sup>29</sup>) is a widely debated form of intervention in neurodegeneration<sup>92,93</sup> and after neurotrauma.<sup>94,95</sup> Such intervention has been proposed to stabilize degenerating axon ends, promote axon outgrowth and reduce scarring,<sup>29,65,96</sup> but perhaps also to protect homeostatic function such as axonal transport.<sup>97</sup> However, in neuroinflammation, microtubule stabilization has not been seen as a promising target, on the one hand because hitherto microtubular changes were described as rather late changes in axon (Sorbara et al.<sup>63</sup>, but cf. Shriver and Dittel<sup>98</sup>), but also because the immunosuppressive effects of microtubule-targeting drugs hamper analysis of direct axonal effects in chronic settings.<sup>99</sup> Indeed, these immunosuppressive effects—as well as chronic neurotoxicity and the possibility of preventing physiological plasticity<sup>100</sup>—make the implementation of microtubule stabilizing therapies in traumatic settings challenging, both acutely and to support long-term recovery. In contrast, we now show that in our NMO model, epothilone (as well as hyperosmotic intervention using mannitol) can largely prevent beading during the acute phase. This result is in line with previously described pearling instability models of axons: when microtubules are disrupted, the threshold tension to form beadings is decreased, as the internal cytoskeletal elastic resistance is altered.<sup>91</sup> The decrease in such elasticity, together with the presence of additional osmotic impact due to the release of the cytosolic components of lysed astrocytes or altered osmotic regulation due to lack of astrocyte end-feet,<sup>89,91</sup> are probably drivers of acute axonal beading. Given the result that the beaded state is relatively long lived, but is eventually followed by potentially destructive calcium dysregulation in a substantial fraction of axons (Fig. 1D and E), a window of opportunity for protective intervention might exist. Considering the time line of our model, microtubule stabilization here is probably acting directly on axons, rather than the immune system, even though, because of the pharmacological nature of the intervention, non-specific effects cannot be ruled out. Even if microtubule stabilization would be found to only transiently protect axons from lasting degeneration, such an intervention could be a useful add-on to combine with subsequent immunomodulatory therapies, as the initial damage in first NMO lesions can be already be severe and debilitating. Thus, microtubule stabilization might have a translational

potential for a short time window, e.g. in the very acute phase of an NMO relapse. Moreover, in an NMO setting, also an acute anti-proliferative effect would be less of a problem, as a course of steroids is part of current standard relapse management anyway.<sup>99</sup> In the context of the experimental setting reported here, however, this translational outlook remains speculative, as our surgical approach to the spinal cord requires dura-opening, which together with the acute and transient nature of our NMO model, makes following the long-term lesion fate in a true therapy experiment impossible. Still, our data provide mechanistic insights that suggest exploring acute disruption of the microtubular cytoskeleton as a worthwhile target for acute axon-protective intervention during a destructive NMO relapse.

## Acknowledgements

We thank M. Budak, N. Budak, P. Apostolopoulos and S. Taskin for animal husbandry and Y. Hufnagel, K. Wullmann, M. Schetterer, V. Grummel, K. Schulz and O. Kowatsch for technical and administrative support. We thank G. Kislinger for EM rendering and reconstruction, and K. Heise for support with the analysis of EM data. The *Aldh111:GFP* mouse strain used for this project [STOCK Tg(*Aldh111-EGFP*)OFC789Gsat/Mmucd; identification no.: 011015-UCD] was obtained from the Mutant Mouse Regional Resource Center, a NCRN-NIH-funded strain repository, and was donated to the MMRR by the NINDS funded GENSAT BAC transgenic project. We thank the Lichtman, Griesbeck and Ding laboratories for their kind sharing of mouse lines (see 'Materials and methods' section for details).

## Funding

This project was supported by the Deutsche Forschungsgemeinschaft (DFG) grant TRR 274/1 2022 (B03 to M.H., C.S. and T.M.; Z01 to M.S.—ID 408885537), as well as under Germany's Excellence Strategy within the framework of the Munich Cluster for Systems Neurology (EXC 2145 SyNergy—ID 390857198; to T.M., B.H. and M.S.) and by the Gemeinnützige Hertie-Stiftung (P1150064 to M.H., B.H. and T.M.; Hertie Network of Excellence in Clinical Neuroscience grant to N.S.). B.H.'s laboratory was further by the EU consortium MultipleMS and the BMBF funded Clinspect-M project. T.M. is supported by European Research Council under the European Union's Seventh Framework Program (grant no. FP/2007-2013; ERC Grant Agreement no.: 616791), the German Center for Neurodegenerative Disease (DZNE) and the DFG (CRC870 A11—ID 118803580, Mi 694/7-1—ID 299370739, Mi 694/8-1—ID 323061152, Mi 694/9-1 A03—ID 428663564, FOR 'Immunostroke'). C.S. was further supported by the Deutsche Forschungsgemeinschaft (DFG) (CRC 43, STA 1389/2-1, STA 1389/5-1, and under Germany's Excellence Strategy, EXC 2067/1—ID 390729940), the Gemeinnützige Hertie-Stiftung, the Deutsche Multiple Sklerose Gesellschaft (DMSG), and the National MS Society (USA). N.S.'s research is supported by a grant from the Deutsche Forschungsgemeinschaft (DFG) research grant (426715780) and by the Gemeinnützige Hertie-Stiftung Network of Excellence in Clinical Neuroscience (P1200019). S.K. received support from the Deutsche Forschungsgemeinschaft (DFG)-funded Graduate School of Systemic Neurosciences (GSC 82—ID 24184143). J.L.B. is supported by the National Institutes of Health (EY022936).

## Competing interests

T.M., S.K., N.S., M.S. and A.W. have no competing interests. M.H. received speaker honoraria from Alexion Company (outside of the submitted work). C.S. served on scientific advisory boards for Roche, Merck and Novartis; she received speaker's honoraria from Roche, Merck and Novartis, and her institution received research grants from Novartis, Roche and medDay. B.H. has served on scientific advisory boards for Novartis; he has served as DMSC member for AllergCare, Polpharma and TG therapeutics; he or his institution have received speaker honoraria from Desitin; his institution received research grants from Regeneron for MS research. He holds part of two patents; one for the detection of antibodies against KIR4.1 in a subpopulation of patients with multiple sclerosis and one for genetic determinants of neutralizing antibodies to interferon. None of these activities causes a conflict of interest relevant to the topic of the study.

## Supplementary material

Supplementary material is available at *Brain* online.

## References

1. Wingerchuk DM, Banwell B, Bennett JL, et al. International consensus diagnostic criteria for neuromyelitis optica spectrum disorders. *Neurology*. 2015;85:177–189.
2. Fujihara K. Neuromyelitis optica spectrum disorders: still evolving and broadening. *Curr Opin Neurol*. 2019;32:385–394.
3. Lennon VA, Wingerchuk DM, Kryzer TJ, et al. A serum autoantibody marker of neuromyelitis optica: Distinction from multiple sclerosis. *Lancet*. 2004;364:2106–2112.
4. Lennon VA, Kryzer TJ, Pittock SJ, Verkman AS, Hinson SR. IgG marker of optic-spinal multiple sclerosis binds to the aquaporin-4 water channel. *J Exp Med*. 2005;202:473–477.
5. Hinson SR, Romero MF, Popescu BF, et al. Molecular outcomes of neuromyelitis optica (NMO)-IgG binding to aquaporin-4 in astrocytes. *Proc Natl Acad Sci USA*. 2012;109:1245–1250.
6. Roemer SF, Parisi JE, Lennon VA, et al. Pattern-specific loss of aquaporin-4 immunoreactivity distinguishes neuromyelitis optica from multiple sclerosis. *Brain*. 2007;130:1194–1205.
7. Misu T, Hoftberger R, Fujihara K, et al. Presence of six different lesion types suggests diverse mechanisms of tissue injury in neuromyelitis optica. *Acta Neuropathol*. 2013;125:815–827.
8. Wingerchuk DM, Pittock SJ, Lucchinetti CF, Lennon VA, Weinshenker BG. A secondary progressive clinical course is uncommon in neuromyelitis optica. *Neurology*. 2007;68:603–605.
9. Combes AJE, Matthews L, Lee JS, et al. Cervical cord myelin water imaging shows degenerative changes over one year in multiple sclerosis but not neuromyelitis optica spectrum disorder. *Neuroimage Clin*. 2017;16:17–22.
10. Levy M, Fujihara K, Palace J. New therapies for neuromyelitis optica spectrum disorder. *Lancet Neurol*. 2021;20:60–67.
11. Jarius S, Paul F, Weinshenker BG, Levy M, Kim HJ, Wildemann B. Neuromyelitis optica. *Nat Rev Dis Primers*. 2020;6:85.
12. Lucchinetti CF, Guo Y, Popescu BF, Fujihara K, Itoyama Y, Misu T. The pathology of an autoimmune astrocytopathy: Lessons learned from neuromyelitis optica. *Brain Pathol*. 2014;24:83–97.
13. Bennett JL, Owens GP. Neuromyelitis optica: Deciphering a complex immune-mediated astrocytopathy. *J Neuroophthalmol*. 2017;37:291–299.

14. Brosnan CF, Raine CS. The astrocyte in multiple sclerosis revisited. *Glia*. 2013;61:453–465.
15. Prineas JW, Lee S. Multiple sclerosis: Destruction and regeneration of astrocytes in acute lesions. *J Neuropathol Exp Neurol*. 2019;78:140–156.
16. Liddel SA, Guttenplan KA, Clarke LE, et al. Neurotoxic reactive astrocytes are induced by activated microglia. *Nature*. 2017;541:481–487.
17. Rothhammer V, Borucki DM, Tjon EC, et al. Microglial control of astrocytes in response to microbial metabolites. *Nature*. 2018;557:724–728.
18. Linnerbauer M, Wheeler MA, Quintana FJ. Astrocyte crosstalk in CNS inflammation. *Neuron*. 2020;108:608–622.
19. Booth HDE, Hirst WD, Wade-Martins R. The role of astrocyte dysfunction in Parkinson's disease pathogenesis. *Trends Neurosci*. 2017;40:358–370.
20. Yun SP, Kam T-I, Panicker N, et al. Block of A1 astrocyte conversion by microglia is neuroprotective in models of Parkinson's disease. *Nat Med*. 2018;24:931–938.
21. Kawachi I, Lassmann H. Neurodegeneration in multiple sclerosis and neuromyelitis optica. *J Neurol Neurosurg Psychiatry*. 2017;88:137–145.
22. Duan T, Smith AJ, Verkman AS. Complement-dependent bystander injury to neurons in AQP4-IgG seropositive neuromyelitis optica. *J Neuroinflammation*. 2018;15:294.
23. Coleman MP, Hoke A. Programmed axon degeneration: From mouse to mechanism to medicine. *Nat Rev Neurosci*. 2020;21:183–196.
24. Nikic I, Merkler D, Sorbara C, et al. A reversible form of axon damage in experimental autoimmune encephalomyelitis and multiple sclerosis. *Nat Med*. 2011;17:495–499.
25. Witte ME, Schumacher A-M, Mahler CF, et al. Calcium influx through plasma-membrane nanoruptures drives axon degeneration in a model of multiple sclerosis. *Neuron*. 2019;101:615–624.e5.
26. Cai H, Zhu J, Zhang N, et al. Subregional structural and connectivity damage in the visual cortex in neuromyelitis optica. *Sci Rep*. 2017;7:41914.
27. Hokari M, Yokoseki A, Arakawa M, et al. Clinicopathological features in anterior visual pathway in neuromyelitis optica. *Ann Neurol*. 2016;79:605–624.
28. Herwerth M, Kalluri SR, Srivastava R, et al. In vivo imaging reveals rapid astrocyte depletion and axon damage in a model of neuromyelitis optica-related pathology. *Ann Neurol*. 2016;79:794–805.
29. Ruschel J, Hellal F, Flynn KC, et al. Axonal regeneration. Systemic administration of ephriline B promotes axon regeneration after spinal cord injury. *Science*. 2015;348:347–352.
30. Brill MS, Lichtman JW, Thompson W, Zuo Y, Misgeld T. Spatial constraints dictate glial territories at murine neuromuscular junctions. *J Cell Biol*. 2011;195:293–305.
31. Mank M, Santos AF, Drenth S, et al. A genetically encoded calcium indicator for chronic in vivo two-photon imaging. *Nat Methods*. 2008;5:805–811.
32. Williams PR, Marincu B-N, Sorbara CD, et al. A recoverable state of axon injury persists for hours after spinal cord contusion in vivo. *Nat Commun*. 2014;5:5683.
33. Bennett JL, Lam C, Kalluri SR, et al. Intrathecal pathogenic anti-aquaporin-4 antibodies in early neuromyelitis optica. *Ann Neurol*. 2009;66:617–629.
34. Bruck W, Porada P, Poser S, et al. Monocyte/macrophage differentiation in early multiple sclerosis lesions. *Ann Neurol*. 1995;38:788–796.
35. Winkler A, Wrzos C, Haberl M, et al. Blood-brain barrier resealing in neuromyelitis optica occurs independently of astrocyte regeneration. *J Clin Invest*. 2021;131:e141694.
36. Schindelin J, Arganda-Carreras I, Frise E, et al. Fiji: An open-source platform for biological-image analysis. *Nat Methods*. 2012;9:676–682.
37. Schneider CA, Rasband WS, Eliceiri KW. NIH Image to ImageJ: 25 years of image analysis. *Nat Methods*. 2012;9:671–675.
38. Davalos D, Lee JK, Smith WB, et al. Stable in vivo imaging of densely populated glia, axons and blood vessels in the mouse spinal cord using two-photon microscopy. *J Neurosci Methods*. 2008;169:1–7.
39. Romanelli E, Sorbara CD, Nikic I, Dagkalis A, Misgeld T, Kerschensteiner M. Cellular, subcellular and functional in vivo labeling of the spinal cord using vital dyes. *Nat Protoc*. 2013;8:481–490.
40. Hildebrand DGC, Cicconet M, Torres RM, et al. Whole-brain serial-section electron microscopy in larval zebrafish. *Nature*. 2017;545(7654):345–349.
41. Kasthuri N, Hayworth KJ, Berger DR, et al. Saturated reconstruction of a volume of neocortex. *Cell*. 2015;162:648–661.
42. Berger DR, Seung HS, Lichtman JW. VAST (volume annotation and segmentation tool): Efficient manual and semi-automatic labeling of large 3D image stacks. *Front Neural Circuits*. 2018;12:88.
43. Misgeld T, Kerschensteiner M. In vivo imaging of the diseased nervous system. *Nat Rev Neurosci*. 2006;7:449–463.
44. Coleman M. Axon degeneration mechanisms: Commonality amid diversity. *Nat Rev Neurosci*. 2005;6:889–898.
45. Friese MA, Schattling B, Fugger L. Mechanisms of neurodegeneration and axonal dysfunction in multiple sclerosis. *Nat Rev Neurol*. 2014;10:225–238.
46. Orem BC, Rajaei A, Stirling DP. IP<sub>3</sub>R-mediated intra-axonal Ca<sup>2+</sup> release contributes to secondary axonal degeneration following contusive spinal cord injury. *Neurobiol Dis*. 2020;146:105123.
47. Schattling B, Steinbach K, Thies E, et al. TRPM4 cation channel mediates axonal and neuronal degeneration in experimental autoimmune encephalomyelitis and multiple sclerosis. *Nat Med*. 2012;18:1805–1811.
48. Friese MA, Craner MJ, Ezensperger R, et al. Acid-sensing ion channel-1 contributes to axonal degeneration in autoimmune inflammation of the central nervous system. *Nat Med*. 2007;13:1483–1489.
49. Kerschensteiner M, Schwab ME, Lichtman JW, Misgeld T. In vivo imaging of axonal degeneration and regeneration in the injured spinal cord. *Nat Med*. 2005;11:572–577.
50. Bruck W, Popescu B, Lucchinetti CF, et al. Neuromyelitis optica lesions may inform multiple sclerosis heterogeneity debate. *Ann Neurol*. 2012;72:385–394.
51. Parratt JD, Prineas JW. Neuromyelitis optica: A demyelinating disease characterized by acute destruction and regeneration of perivascular astrocytes. *Mult Scler*. 2010;16:1156–1172.
52. Weil MT, Mobius W, Winkler A, et al. Loss of myelin basic protein function triggers myelin breakdown in models of demyelinating diseases. *Cell Rep*. 2016;16:314–322.
53. Drawitsch F, Karimi A, Boergens KM, Helmstaedter M. FluoEM, virtual labeling of axons in three-dimensional electron microscopy data for long-range connectomics. *eLife*. 2018;7:e38976.
54. Waxman SG, Bennett MV. Relative conduction velocities of small myelinated and non-myelinated fibres in the central nervous system. *Nat New Biol*. 1972;238:217–219.

55. Greenberg MM, Leitao C, Trogadis J, Stevens JK. Irregular geometries in normal unmyelinated axons: a 3D serial EM analysis. *J Neurocytol.* 1990;19:978–988.
56. Beirowski B, Nogradi A, Babetto E, Garcia-Alias G, Coleman MP. Mechanisms of axonal spheroid formation in central nervous system Wallerian degeneration. *J Neuropathol Exp Neurol.* 2010; 69:455–472.
57. Coleman MP, Freeman MR. Wallerian degeneration, wld(s), and nmnat. *Annu Rev Neurosci.* 2010;33:245–267.
58. Osterloh JM, Yang J, Rooney TM, et al. dSarm/Sarm1 is required for activation of an injury-induced axon death pathway. *Science.* 2012;337:481–484.
59. Geden MJ, Deshmukh M. Axon degeneration: Context defines distinct pathways. *Curr Opin Neurobiol.* 2016;39:108–115.
60. Hertz NT, Adams EL, Weber RA, et al. Neuronally enriched RUFY3 is required for caspase-mediated axon degeneration. *Neuron.* 2019;103:412–422.e4.
61. Maday S, Twelvetrees AE, Moughamian AJ, Holzbaur EL. Axonal transport: Cargo-specific mechanisms of motility and regulation. *Neuron.* 2014;84:292–309.
62. Papadopoulos MC, Verkman AS. Aquaporin water channels in the nervous system. *Nat Rev Neurosci.* 2013;14:265–277.
63. Sorbara CD, Wagner NE, Ladwig A, et al. Pervasive axonal transport deficits in multiple sclerosis models. *Neuron.* 2014; 84:1183–1190.
64. Brunden KR, Lee VM-Y, Smith AB III, Trojanowski JQ, Ballatore C. Altered microtubule dynamics in neurodegenerative disease: Therapeutic potential of microtubule-stabilizing drugs. *Neurobiol Dis.* 2017;105:328–335.
65. Hellal F, Hurtado A, Ruschel J, et al. Microtubule stabilization reduces scarring and causes axon regeneration after spinal cord injury. *Science.* 2011;331:928–931.
66. Verkhratsky A, Sofroniew MV, Messing A, et al. Neurological diseases as primary gliopathies: A reassessment of neurocentrism. *ASN Neuro.* 2012;4:e00082.
67. Pekny M, Pekna M, Messing A, et al. Astrocytes: A central element in neurological diseases. *Acta Neuropathol.* 2016;131: 323–345.
68. Chen T, Lennon VA, Liu YU, et al. Astrocyte-microglia interaction drives evolving neuromyelitis optica lesion. *J Clin Invest.* 2020;130:4025–4038.
69. Tradtrantip L, Asavapanumas N, Verkman AS. Emerging therapeutic targets for neuromyelitis optica spectrum disorder. *Expert Opin Ther Targets.* 2020;24:219–229.
70. Coleman MP, Perry VH. Axon pathology in neurological disease: A neglected therapeutic target. *Trends Neurosci.* 2002; 25:532–537.
71. Raff MC, Whitmore AV, Finn JT. Axonal self-destruction and neurodegeneration. *Science.* 2002;296:868–871.
72. Nitsch R, Pohl EE, Smorodchenko A, Infante-Duarte C, Aktas O, Zipp F. Direct impact of T cells on neurons revealed by two-photon microscopy in living brain tissue. *J Neurosci.* 2004;24:2458–2464.
73. Knoferle J, Koch JC, Ostendorf T, et al. Mechanisms of acute axonal degeneration in the optic nerve in vivo. *Proc Natl Acad Sci USA.* 2010;107:6064–6069.
74. Stirling DP, Cummins K, Wayne Chen SR, Stys P. Axoplasmic reticulum Ca<sup>(2+)</sup> release causes secondary degeneration of spinal axons. *Ann Neurol.* 2014;75:220–229.
75. Ouardouz M, Nikolaeva MA, Coderre E, et al. Depolarization-induced Ca<sup>2+</sup> release in ischemic spinal cord white matter involves L-type Ca<sup>2+</sup> channel activation of ryanodine receptors. *Neuron.* 2003;40:53–63.
76. Stirling DP, Stys PK. Mechanisms of axonal injury: Internodal nanocomplexes and calcium deregulation. *Trends Mol Med.* 2010;16:160–170.
77. Stys PK. Anoxic and ischemic injury of myelinated axons in CNS white matter: From mechanistic concepts to therapeutics. *J Cereb Blood Flow Metab.* 1998;18:2–25.
78. Yang J, Weimer RM, Kallop D, et al. Regulation of axon degeneration after injury and in development by the endogenous calpain inhibitor calpastatin. *Neuron.* 2013;80:1175–1189.
79. Wolf JA, Stys PK, Lusardi T, Meaney D, Smith DH. Traumatic axonal injury induces calcium influx modulated by tetrodotoxin-sensitive sodium channels. *J Neurosci.* 2001; 21:1923–1930.
80. Waxman SG. Axonal conduction and injury in multiple sclerosis: the role of sodium channels. *Nat Rev Neurosci.* 2006;7: 932–941.
81. Trapp BD, Stys PK. Virtual hypoxia and chronic necrosis of demyelinated axons in multiple sclerosis. *Lancet Neurol.* 2009; 8:280–291.
82. Court FA, Coleman MP. Mitochondria as a central sensor for axonal degenerative stimuli. *Trends Neurosci.* 2012;35:364–372.
83. Tradtrantip L, Yao X, Su T, Smith AJ, Verkman AS. Bystander mechanism for complement-initiated early oligodendrocyte injury in neuromyelitis optica. *Acta Neuropathol.* 2017; 134:35–44.
84. Bruck W, Bruck Y, Diederich U, Piddlesden SJ. The membrane attack complex of complement mediates peripheral nervous system demyelination in vitro. *Acta Neuropathol.* 1995;90:601–607.
85. Serna M, Giles JL, Morgan BP, Bubeck D. Structural basis of complement membrane attack complex formation. *Nat Commun.* 2016;7:10587.
86. Singh S, Dallenga T, Winkler A, et al. Relationship of acute axonal damage, Wallerian degeneration, and clinical disability in multiple sclerosis. *J Neuroinflammation.* 2017;14:57.
87. Vargas ME, Yamagishi Y, Tessier-Lavigne M, Sagasti A. Live imaging of calcium dynamics during axon degeneration reveals two functionally distinct phases of calcium influx. *J Neurosci.* 2015;35:15026–15038.
88. Ochs S, Pourmand R, Jersild RA Jr, Friedman RN. The origin and nature of beading: A reversible transformation of the shape of nerve fibers. *Prog Neurobiol.* 1997;52:391–426.
89. Pullarkat PA, Dommersnes P, Fernandez P, Joanny J-F, Ott A. Osmotically driven shape transformations in axons. *Phys Rev Lett.* 2006;96:048104.
90. Ochs S, Jersild RA Jr. Cytoskeletal organelles and myelin structure of beaded nerve fibers. *Neuroscience.* 1987;22:1041–1056.
91. Datar A, Ameeramja J, Bhat A, et al. The roles of microtubules and membrane tension in axonal beading, retraction, and atrophy. *Biophys J.* 2019;117:880–891.
92. Zhang B, Carroll J, Trojanowski JQ, et al. The microtubule-stabilizing agent, epothilone D, reduces axonal dysfunction, neurotoxicity, cognitive deficits, and Alzheimer-like pathology in an interventional study with aged tau transgenic mice. *J Neurosci.* 2012;32:3601–3611.
93. Ballatore C, Brunden KR, Huryn DM, Trojanowski JQ, Lee VM-Y, Smith AB III. Microtubule stabilizing agents as potential treatment for Alzheimer's disease and related neurodegenerative tauopathies. *J Med Chem.* 2012;55: 8979–8996.
94. Griffin JM, Bradke F. Therapeutic repair for spinal cord injury: Combinatory approaches to address a multifaceted problem. *EMBO Mol Med.* 2020;12:e11505.



95. Curcio M, Bradke F. Axon regeneration in the central nervous system: Facing the challenges from the inside. *Annu Rev Cell Dev Biol.* 2018;34:495–521.
96. Erturk A, Hellal F, Enes J, Bradke F. Disorganized microtubules underlie the formation of retraction bulbs and the failure of axonal regeneration. *J Neurosci.* 2007;27:9169–9180.
97. Fernandez-Valenzuela JJ, Sanchez-Varo R, Munoz-Castro C, et al. Enhancing microtubule stabilization rescues cognitive deficits and ameliorates pathological phenotype in an amyloidogenic Alzheimer's disease model. *Sci Rep.* 2020;10:14776.
98. Shriver LP, Dittel BN. T-cell-mediated disruption of the neuronal microtubule network: correlation with early reversible axonal dysfunction in acute experimental autoimmune encephalomyelitis. *Am J Pathol.* 2006;169:999–1011.
99. O'Sullivan D, Miller JH, Northcote PT, La Flamme AC. Microtubule-stabilizing agents delay the onset of EAE through inhibition of migration. *Immunol Cell Biol.* 2013;91:583–592.
100. Brill MS, Kleele T, Ruschkies L, et al. Branch-specific microtubule destabilization mediates axon branch loss during neuromuscular synapse elimination. *Neuron.* 2016;92:845–856.